Spectral collocation methods for polymer brushes

Tanya L. Chantawansri,[1,2] Su-Mi Hur,[1] Carlos J. García-Cervera,[3] Hector D. Ceniceros,[3] and Glenn H. Fredrickson[1,4,5,a)]

[1)] *Department of Chemical Engineering, University of California, Santa Barbara, California 93106 USA*

[2)] *The U.S. Army Research Laboratory, Aberdeen Proving Grounds, MD 21005 USA*

[3)] *Department of Mathematics, University of California, Santa Barbara, California 93106 USA*

[4)] *Materials Research Laboratory, University of California, Santa Barbara, California 93106 USA*

[5)] *Department of Materials, University of California, Santa Barbara, California 93106 USA*

(Dated: 2 June 2011)

We provide an in-depth study of pseudo-spectral numerical methods associated with modeling the self-assembly of molten mixed polymer brushes in the framework of self-consistent field theory (SCFT). SCFT of molten polymer brushes has proved numerically challenging in the past because of sharp features that arise in the self-consistent pressure field at the grafting surface due to the chain end tethering constraint. We show that this pressure anomaly can be reduced by smearing the grafting points over a narrow zone normal to the surface in an incompressible model, and/or by switching to a compressible model for the molten brush. In both cases, we use results obtained from a source (delta function) distribution of grafting points as a reference. At the grafting surface, we consider both Neumann and Dirichlet conditions, where the latter is paired with a masking method to mimic a confining surface. When only the density profiles and relative free energies of two comparison phases are of interest, either source or smeared distributions of grafting points can be used, but a smeared distribution of grafting points exhibits faster convergence with respect to the number of chain contour steps. Absolute free energies converge only within the smeared model. In addition, when a sine basis is used with the masking method and a smeared distribution, fewer iterations are necessary to converge the SCFT fields for the compressible model. The numerical methods described here and investigated in one-dimension will provide an enabling platform for computationally more demanding three-dimensional SCFT studies of a broad range of mixed polymer brush systems.

[a)] Author to whom correspondence should be addressed. Electronic email:ghf@mrl.ucsb.edu

I. INTRODUCTION

Polymer brushes are comprised of polymer chains that are tethered by one end to a surface or interface on the 10 nanometer length scale[6,11,13,31]. Broad interest in polymer brushes exists due to their uses in a variety of applications, such as colloidal stabilization, membrane surface modification, biocompatible surfaces for medicine, tunable and switchable surfaces, and templates for advanced microelectronic devices[15,17,46,51]. Polymer brushes can be further classified as being either "pure" or "mixed". A pure brush is composed of a single type of end-grafted polymer; such a brush may either be in a dense liquid state (melt brush), or swollen by a solvent (solution brush). In contrast, mixed brushes contain two or more chemically dissimilar polymers that are end-tethered to a surface. Mixed brushes can also be molten or solvated and can possess a rich variety of microphase separation behavior as dissimilar segments spatially segregate under the constraints imposed by the grafting surface and the interactions of the components with the free surface of the brush (usually air or solvent)[19]. The present paper relates to numerical methods that can be used to predict the self-assembly and microphase separation behavior of such mixed polymer brushes.

A powerful theoretical and computational tool for describing inhomogeneous polymer melts and solutions is self-consistent field theory (SCFT)[9,24]. The SCFT construct is built around field-theoretic models of interacting polymer systems, which are analyzed using a simplifying "mean-field" approximation that comprises a saddle point approximation to the functional integrals that define the partition function of a model. The resulting mean-field or SCFT equations are highly nonlocal and nonlinear equations that can nonetheless be tackled by a variety of spectral, pseudo-spectral, or real-space methods[3,8,9,28,29]. Numerical implementations of SCFT have shown widespread success in anticipating and explaining the self-assembly characteristics of a wide range of complex polymer systems including polymer alloys, block and graft copolymers, polymer solutions, supramolecular polymers, and thin films[7,9,14,22,24,29].

Most of the early computational work on polymer brushes was conducted using a type of lattice mean-field theory known as the Scheutjens-Fleer model[44,50]. While this has proved to be a successful and simple approach for modeling brushes, such lattice methods can be computationally expensive for high resolution, high dimensional simulations, and can result in broken symmetries due to the lattice discretization of space. Even so, the Scheutjens-

Fleer lattice model has been used to model a variety of systems, including pure and mixed brushes in planar geometries[4,39].

In contrast to the Scheutjens-Fleer model, SCFT models are formulated in continuous space with continuous chain models, such as the continuous Gaussian chain model. In the latter, polymers are modeled as elastic threads with no penalty for bending and a local harmonic stretching energy[9]. Continuum models of polymer brushes can be easily constructed in this framework by tethering the ends of the elastic threads to a grafting surface. In the limit of high grafting density, where polymers must stretch away from the surface in order to avoid overlap, a further analytical simplification of the SCFT equations can be made. In this so-called "classical" or "strong stretching theory" (SST), the path integral comprising the partition function of a polymer strand is approximated (by analogy with the path integral formulation of quantum mechanics) by the classical path[32–34,45]. Although many insights have been gained by SST calculations, most experimental systems fall in the weakly or moderately stretched categories. In spite of considerable effort made to correct the SST model, where the entropy associated with the free chain ends of the brush, along with corrections due to a proximal layer near the grafting surface were both incorporated[18,21,23,26,38], numerical approaches are necessary to study more realistic and complex systems. Notably, the *inhomogeneous* mixed brushes of primary interest here are largely inaccessible by analytical SST methods.

The full SCFT equations for pure and mixed polymer brushes have also been attacked by a variety of numerical methods including real-space finite differences, Matsen's fully spectral (Galerkin) method, and pseudo-spectral (collocation) techniques. Specifically, brushes have been studied using the fully spectral method by Müller[35], Matsen[23], Matsen and Gardiner[27], and Matsen and Griffiths[25], while the pseudo-spectral method was employed by Meng *et al*[30]. Although the numerical methods required to solve the SCFT equations for a brush are much the same as for non-tethered polymeric systems such as blends and block copolymers, there is a special difficulty in the case of brushes arising from the grafting constraint. In particular, the polymer propagator used to sum over the paths emerging from a point on the grafting surface has a Dirac delta distribution initial condition constraining the chain end to the surface. This is problematic because the propagator, which satisfies a type of diffusion equation, must be adequately resolved in both space and time (a fictitious time along the chain contour) to enable accurate evaluation of polymer structures and free energies. Matsen

et al.[26,27] observed that a partially resolved delta function initial condition, in concert with a reflective boundary condition at the grafting surface and the assumption of incompressibility in a melt brush, produces a cusp in the self-consistent fields near the grafting surface. This singular feature was observed to seriously deteriorate the convergence properties of Galerkin spectral methods. The cusp was further analyzed for a one-component melt brush and was attributed to the proximal layer, where an over expression of monomers near the substrate produces an elevated density that is compensated by a singular pressure profile[26,27]. As we detail below, this cusp exists irrespective of the boundary conditions applied at the grafting surface and seems to be an artifact of the use of a continuous chain model and the strict application of incompressibility.

Matsen argued that a delta function should be included in the pressure field of an incompressible model at the surface to compensate for the elevated segment density created by grafting. Rather than attempting to numerically resolve that contribution, he argued for an effective Robin type boundary condition on the propagator that approximately cancels the singularity in the pressure. In practice, this approach suppresses, but does not completely eliminate, the pressure anomaly[26,27]. While Robin boundary conditions can be easily implemented in the fully spectral formalism, we have found them to be problematic in pseudo-spectral methods that are desirable for large-scale simulations of polymer brushes implemented with parallel fast Fourier transforms (FFTs). The use of a Chebyshev basis in principle allows for the imposition of Robin conditions in an FFT framework, but Robin boundary conditions are not convenient in mixed brush systems where one would like to access a broad variety of interactions between the substrate and the multiple segment species of the brush.

Meng et al.[30] also observed numerical instabilities associated with the delta function initial condition when the SCFT equations for an incompressible melt are solved by spectral collocation and Dirichlet boundary conditions at the grafting surface. These workers tried to circumvent the problem by calculating the first few contour steps of the propagators using a corresponding integral equation (a Chapman-Kolmogorov equation) before switching to the modified diffusion equation for the remainder of the chain. Even so, we found that such a technique alone does not resolve the pressure anomaly.

To address these various issues, in this paper we investigate spectral collocation using sine and cosine bases to solve the SCFT equations for mixed polymer brushes, using both

compressible and incompressible models. In the sine basis case, we simultaneously specify a mask or wall function[9,20] which is necessary in the incompressible model to relieve an incompatibility with the use of a homogeneous Dirichlet condition on the polymer propagators. The mask also provides a convenient way to impose selective wetting conditions of the brush components at the grafting surface. To address the pressure anomaly, a smeared distribution of grafting points normal to the substrate is investigated and results are compared to a point source distribution modeled with a Dirac delta function. By using this method, we will show that convergence problems associated with the grafting constraint are alleviated and quantities such as densities and free energies can be evaluated to high precision.

II. MODEL

In the present manuscript, we consider a two-component AB mixed polymer brush where the A and B homopolymers are modeled as continuous elastic filaments by means of the continuous Gaussian chain model. The theoretical construct will be self-consistent field theory (SCFT), which uses a mean-field, saddle point approximation to evaluate the functional integrals that appear in equilibrium statistical field theory models of inhomogeneous polymers. Below we summarize the relevant equations and relaxation methods. Further details about the derivation can be obtained from the monograph by Fredrickson[9].

In the system under investigation, the brush is composed of n_A and n_B monodisperse A and B tethered homopolymers bounded by n_w "wall" particles in a volume V at an average segment and wall particle density of $\rho_0 = (n_A N + n_B N + n_w)/V$. The statistical segment lengths of the polymers ($b_A = b_B = b$) and the indices of polymerization ($N_A = N_B = N$) are assumed to be equal for both components. The immobile wall particles are introduced as a construct for implementing a mask as discussed below. One end of the A and B polymers is grafted permanently to a planar surface of area $\mathcal{A}$ at a grafting density of $\sigma_A = n_A/\mathcal{A} = fn/\mathcal{A}$ and $\sigma_B = n_B/\mathcal{A} = (1-f)n/\mathcal{A}$, respectively, where f is the volume fraction of A segments and $n = n_A + n_B$. The chemical incompatibility of the two homopolymers are modeled with a Flory-type monomer-monomer interaction parameter χ.

For the case of Dirichlet boundary conditions, we employ a masking method at the bottom and top surfaces of the brush to confine the polymer segments and define finite-width interfaces over which the segment density rises from zero to the bulk value in the brush.

This renders Dirichlet conditions on the propagators compatible with the incompressible melt and allows for the imposition of surface affinities for selective components[2,14,20]. Wall particles distributed with specified volume fractions, $\phi_{w1}(\mathbf{x})$ and $\phi_{w2}(\mathbf{x})$, are introduced to model the grafting and top surfaces, respectively, and a penalty function is introduced to exclude the polymer segments from the boundary wall confinement regions. The wall particles interact with the A and B segments through Flory-like interaction parameters, χ_{wA} and χ_{wB}, respectively. In an incompressible model, the wetting characteristics of the wall are dictated by the single parameter $\chi_w \equiv -(\chi_{wA}-\chi_{wB})/2$, where positive and negative values correspond to A and B attractive walls, respectively. For the compressible model, we arbitrarily set $\chi_{wA}+\chi_{wB}=0$ as a second condition, so that χ_w is again the single parameter controlling wetting behavior. Since two walls are present, this parameter is separately defined for the grafting substrate and grafting-free surface (opposite the grafting surface) as χ_{w1} and χ_{w2}, respectively.

In addition to the harmonic stretching energy of the Gaussian chain and the segment interaction energy, a penalty for local density fluctuations away from the average density, ρ_0, is modeled using either an incompressible or compressible model. For the incompressible model, which is commonly used for melt systems, a local incompressibility constraint is imposed by using a delta functional such as

$$\delta\left[\sum_i \hat{\rho}_i(\mathbf{r}) - \rho_0\right], \tag{1}$$

at each point $\mathbf{r}$ where $\hat{\rho}_i(\mathbf{r})$ is the microscopic segment density of species i. In the compressible model a harmonic functional energetic term is included in the partition function in place of the local incompressibility constraint:

$$e^{-\frac{\zeta}{2\rho_0}\int_V d\mathbf{r}\left(\sum_i \hat{\rho}_i(\mathbf{r})-\rho_0\right)^2}, \tag{2}$$

where ζ corresponds to a penalty for local density fluctuations away from the average density ρ_0, such that in the limit $\zeta \to \infty$, it approaches the incompressible model. The polymer-polymer interactions are decoupled in favor of field-polymer interactions by means of Hubbard-Stratonovich transformations, which introduce a *pressure* field μ_+ and an *exchange* or *composition* field μ_-. The field-theoretic Hamiltonian takes the following form

$$H[\mu_+,\mu_-] = C\int_{\bar{V}} d\mathbf{x}\left[-\mu_+(\mathbf{x})\phi(\mathbf{x}) - \frac{2\mu_-(\mathbf{x})}{\chi N}\left(\chi_{w1}N\phi_{w1}(\mathbf{x}) + \chi_{w2}N\phi_{w2}(\mathbf{x})\right) + (2f-1)\mu_-(\mathbf{x})\right.$$
$$\left.+\mu_-^2(\mathbf{x})/\chi N\right] - \frac{Cf\bar{\phi}\bar{V}}{\bar{\mathcal{A}}}\int_{\bar{\mathcal{A}}} d\mathbf{x}_\perp \log\mathcal{Q}(\mathbf{x}_\perp;[\mu_A]) - \frac{C(1-f)\bar{\phi}\bar{V}}{\bar{\mathcal{A}}}\int_{\bar{\mathcal{A}}} d\mathbf{x}_\perp \log\mathcal{Q}(\mathbf{x}_\perp;[\mu_B]). \quad (3)$$

for the incompressible model. The Hamiltonian for the compressible model is obtained by replacing the first term inside the integral, $-\mu_+(\mathbf{x})\phi(\mathbf{x})$, with $-\frac{1}{\chi N+2\zeta N}\mu_+^2(\mathbf{x}) - \frac{2\zeta N}{\chi N+2\zeta N}\phi(\mathbf{x})\mu_+(\mathbf{x})$. Here, we introduced new dimensionless variables, $\mathbf{x} = \mathbf{r}/R_{g0}$, $\bar{V} = V/R_{g0}^3$, $\bar{\mathcal{A}} = \mathcal{A}/R_{g0}^2$, each scaled by the polymer radius of gyration, $R_{g0} = b(N/6)^{1/2}$. The dimensionless polymer chain concentration is denoted by $C = \rho_0 R_{g0}^3/N$ and the spatial average of the total (A and B) polymer volume fraction, $\phi(\mathbf{x})$, is designated as $\bar{\phi}$. An integral over grafting points $\mathbf{x}_\perp$ on the substrate is denoted by $\int_{\bar{\mathcal{A}}} d\mathbf{x}_\perp$.

In Eq. (3), the normalized single chain partition function for a polymer chain tethered to the grafting point, $\mathbf{x}_\perp$, $\mathcal{Q}(\mathbf{x}_\perp;[\mu_K])$, can be calculated through

$$\mathcal{Q}(\mathbf{x}_\perp, s;[\mu_K]) = \int_{\bar{V}} d\mathbf{x}\; q_{\mathbf{x}_\perp}(\mathbf{x}, s;[\mu_K])q(\mathbf{x}, 1-s;[\mu_K]) \quad (4)$$

for component $K = A$ or B and arbitrary contour location s, where $q_{\mathbf{x}_\perp}(\mathbf{x}, s;[\mu_K])$ is the chain propagator initiated from the grafting plane, and $q(\mathbf{x}, s;[\mu_K])$ is the propagator initiated from the free-end.

The free-end propagator, $q(\mathbf{x}, s;[\mu_K])$, is the probability that a polymer chain of contour length s has its end located at spatial position, $\mathbf{x}$. It can be obtained by solving the following modified diffusion equation

$$\frac{\partial}{\partial s}q(\mathbf{x}, s;[\mu_K]) = \nabla^2 q(\mathbf{x}, s;[\mu_K]) - \mu_K(\mathbf{x})q(\mathbf{x}, s;[\mu_K]), \quad (5)$$

where the $\mu_K(\mathbf{x})$ are the potential fields experienced by segments of type K:

$$\begin{aligned}\mu_A(\mathbf{x}) &= \mu_+(\mathbf{x}) - \mu_-(\mathbf{x})\\ \mu_B(\mathbf{x}) &= \mu_+(\mathbf{x}) + \mu_-(\mathbf{x}),\end{aligned} \quad (6)$$

The free end propagator is subject to the initial condition $q(\mathbf{x}, 0;[\mu_K]) = 1$.

The chain propagator initiating from the grafting point $\mathbf{x}_\perp$, denoted as $q_{\mathbf{x}_\perp}(\mathbf{x}, s;[\mu_K])$, also satisfies the modified diffusion equation (5) but its initial condition takes into account the distribution of grafting points. For a chain grafted at point $\mathbf{x}_\perp$, the local volume fraction contributed by that chain and the overall chain partition function are also functions of $\mathbf{x}_\perp$.

With a high and uniform grafting density assumption, the quenched average over chain end grafting points is affected by the integrals in Eq. (3) over the grafting surface. However, the surface integral can be absorbed into the initial condition for a new averaged propagator originating from the surface called the *complementary* propagator $q_c(\mathbf{x}, s, [\mu_K])$[35–37]. This object also satisfies Eq. (5), but with the following initial conditions for species A and B, respectively:

$$q_c(\mathbf{x}, 0; [\mu_A]) = \int_{\bar{\mathcal{A}}} d\mathbf{x}_\perp \frac{f\bar{V}}{\bar{\mathcal{A}}\mathcal{Q}(\mathbf{x}_\perp; [\mu_A])} q_{\mathbf{x}_\perp}(\mathbf{x}, 0; [\mu_A]), \tag{7}$$

$$q_c(\mathbf{x}, 0; [\mu_B]) = \int_{\bar{\mathcal{A}}} d\mathbf{x}_\perp \frac{(1-f)\bar{V}}{\bar{\mathcal{A}}\mathcal{Q}(\mathbf{x}_\perp; [\mu_B])} q_{\mathbf{x}_\perp}(\mathbf{x}, 0; [\mu_B]). \tag{8}$$

To calculate the local volume fraction of species K, the following expression can be used:

$$\phi_K(\mathbf{x}; [\mu_K]) = \bar{\phi} \int_0^1 ds\ q_c(\mathbf{x}, s; [\mu_K])\ q(\mathbf{x}, 1-s; [\mu_K]), \tag{9}$$

For the incompressible model, the mean-field configurations of the pressure and exchange field are determined from the following saddle-point equations:

$$\frac{\delta H[\mu_+, \mu_-]}{\delta \mu_+(\mathbf{x})} = \phi_A(\mathbf{x}; [\mu_A^*]) + \phi_B(\mathbf{x}; [\mu_B^*]) - \phi(\mathbf{x}) = 0, \tag{10}$$

and

$$\begin{aligned} \frac{\delta H[\mu_+, \mu_-]}{\delta \mu_-(\mathbf{x})} = (2f-1) + \frac{2\mu_-^*(\mathbf{x})}{\chi N} - \frac{2\chi_{w1}N}{\chi N}\phi_{w1}(\mathbf{x}) \\ - \frac{2\chi_{w2}N}{\chi N}\phi_{w2}(\mathbf{x}) - \phi_A(\mathbf{x}; [\mu_A^*]) \\ + \phi_B(\mathbf{x}; [\mu_B^*]) = 0, \end{aligned} \tag{11}$$

where μ_+^* and μ_-^* denotes the values of the fields at the saddle point. For the compressible model, the last term $-\phi(\mathbf{x})$ in Eq. (10) is replaced by $\left(-\frac{2}{\chi N + 2\zeta N}\mu_+^*(\mathbf{x}) - \frac{2\zeta N}{\chi N + 2\zeta N}\phi(\mathbf{x})\right)$.

III. NUMERICAL METHODS

To obtain the mean-field configurations for μ_+ and μ_-, we use the following iterative scheme:

1. Initialize the fields, μ_+ and μ_-.

2. Solve the modified diffusion equation for both q and q_c.

3. Calculate $\mathcal{Q}$, ϕ_A and ϕ_B.

4. Update the fields, μ_+ and μ_-.

5. Repeat steps 2-5 until a convergence criterion is satisfied (when the l_1 norm of the sum of the saddle point equations is at machine precision).

In this section, we describe the numerical methods used to calculate these quantities within the scope of the pseudo-spectral method, with particular attention to the complications arising from the grafting of the polymers to a surface. Moreover, we restrict attention to a one-dimensional planar mixed brush system where pressure and composition variations occur normal to the grafting plane $z \in [0, \bar{L}_z]$. Two different set of boundary conditions are considered: homogeneous Neumann and homogeneous Dirichlet conditions. The numerical methods presented in this manuscript can be easily adapted to a multidimensional system.

Neumann (reflective) boundary conditions are appropriate when it is desired to model a neutral surface for the two polymers at the grafting and free surfaces of the brush. In this case, the wall particles are omitted and no mask is applied. This is achieved by setting $n_w = 0$, $\phi_{w1}(\mathbf{x}) = 0$, and $\phi_{w2}(\mathbf{x}) = 0$ in the model described in Section II. Correspondingly, the average polymer volume fraction is $\bar{\phi} = 1$.

To model surface affinity for type A or B segments at the boundaries, we introduce masks at each surface coupled with Dirichlet boundary conditions; this is similar to the work on lateral confinement of block copolymers in[14]. Although we consider Neumann boundary conditions for a neutral surface, a surface affinity can be added as a local or finite-range interaction. In the case of Dirichlet boundary conditions, the wall volume fraction, $\phi_w(z)$, is defined such that its value is one at the boundary and decays to zero into the brush over a length d much less than the brush thickness $\bar{L}_z$. At the grafting surface $z = 0$, we make the simple choice $\phi_{w1}(z) = [1+\cos(\pi z/d)]/2$; at the grafting-free surface we similarly choose $\phi_{w2}(z) = [1+\cos(\pi(\bar{L}_z - z)/d)]/2$. This wall profile has the desirable properties that its first derivative is peaked a distance $d/2$ from the wall and is zero both at the wall and at $z = d$. The function $(\phi_w^{'}(z))^2$, when normalized, is therefore a convenient choice as a distribution function for smearing the grafting points throughout the wall region. This will be described further in Section III B. Bosse et al.[2] observed that the value of d, i.e. the wall interface width, does not affect mesoscopic polymer assembly as long as it is set below the scale of R_{g0}. For the moderately stretched brushes considered in this manuscript, which are only a few

multiples of R_{g0} thick, the volume of the wall region is a non-negligible fraction of the overall brush volume. Thus, most comparisons are made at the same value of d, and in comparing results at different brush thicknesses, we also maintain the same spatial resolution to ensure consistent resolution of the wall regions.

In our study, we use spectral collocation with a sine or cosine basis and a uniform collocation grid in the spatial coordinate z. We also apply equispaced points in the s chain contour variable. The number of collocation points and chain contour steps are denoted by N_z and N_s, respectively.

A. Modified Diffusion Equation

The most computationally expensive step in the SCFT method involves solving the modified diffusion equation for the chain propagators, q and q_c. In this section, three different second-order accurate methods that can be used to calculate these objects are discussed: an operator splitting method, a backwards differentiation formula, and an exponential differentiation formula. All of these methods require transformations between real and spectral/Fourier space. To efficiently transform between the values of functions $f(z)$ sampled on a uniform grid and its cosine ($\hat{f}_m$) and sine ($\breve{f}_m$) Fourier coefficients, the FFTW package is used[10], where the cosine and sine transforms are denoted by REDFT00(DCT-I) and RODFT00(DST-I), respectively. The inverse transforms are given by the same routines, but are normalized by multiplying by $1/(2(N_z-1))$ or $1/(2(N_z+1))$ for the cosine or sine transforms, respectively.

1. Operator Splitting Method (OSM)

An attractive way to solve the modified diffusion equations is the pseudo-spectral operator splitting method (OSM)[9,41,48,49]. This is an unconditionally stable, fast, $\mathcal{O}(\Delta s^2)$ accurate algorithm for solving the modified diffusion equations. In Eq. (5), we can identify a linear operator $\mathcal{L} = \nabla^2 - \mu(z)$, where in the current 1D case $\nabla^2 = \partial_z^2$. Values of $q(z,s)$ can be calculated at a set of discrete contour points, s, by propagating forward along the polymer contour according to

$$q(z, s+\Delta s) = e^{\Delta s \mathcal{L}} q(z,s), \tag{12}$$

starting from an initial condition $q(z,0) = 1$. The OSM algorithm is based on the Baker-Campbell-Hausdorff identity[43], which affects an $\mathcal{O}(\Delta s^2)$ accurate splitting of $e^{\Delta s \mathcal{L}}$:

$$e^{\Delta s \mathcal{L}} = e^{-\Delta s \mu(z)/2} e^{\Delta s \partial^2/\partial z^2} e^{-\Delta s \mu(z)/2} + \mathcal{O}(\Delta s^3). \tag{13}$$

This equation is solved by spectral collocation[12], transforming between real space and Fourier space with FFTs. Since the potential field $\mu(z)$ is diagonal on a uniform collocation grid in real space for a planar system, and the Laplacian operator is diagonal in Fourier space (sine or cosine basis), the three operators appearing on the right hand side of Eq. (13) can be applied as local multiplications in the appropriate space.

2. *Backwards Differentiation Formula (BDF)*

The backwards differentiation formula (BDF) is a multistep, implicit-explicit scheme. In terms of the modified diffusion equation, this method implicitly treats the Laplacian term and explicitly treats the source using an Adams-Bashforth formula. In other contexts, this method has shown remarkable features, such as improved stability properties and high frequency damping that can reduce aliasing in low resolution simulations[1,42].

The second-order BDF (BDF2) scheme applied to Eq. (5) takes the following form:

$$\begin{aligned} &\frac{1}{2\Delta s}\left[3q(z,s+\Delta s) - 4q(z,s) + q(z,s-\Delta s)\right] = \\ &\nabla^2 q(z,s+\Delta s) - \mu(z)[2q(z,s) - q(z,s-\Delta s)] + \mathcal{O}(\Delta s^3). \end{aligned} \tag{14}$$

To initialize this scheme, the first step is taken using a first-order accurate Euler method, and then Richardson extrapolation[40] is used to produce a second-order accurate value for $q(z,\Delta s)$.

3. *Exponential Differential Formula (EDF)*

Exponential time differencing is another method commonly used to solve stiff ordinary and partial differential equations. This method first involves an exact integration of the equations through the use of an integrating factor. Any integrals with nonlinear parts are then approximated through a Taylor expansion up to a desired order[5]. Although this method can thus be used to obtain schemes of arbitrary order[16], only the second-order method applied to Eq. (5) will be presented.

The second-order accurate exponential differential formula (EDF) is defined by:

$$q(z,s+\Delta s) = L_1 q(z,s) + L_2(\mu(z)q(z,s)) \\ +L_3(\mu(z)q(z,s-\Delta s)) + \mathcal{O}(\Delta s^3) \tag{15}$$

$$L_1 = e^{\Delta s \partial^2/\partial z^2} \tag{16}$$

$$L_2 = \left(\frac{\partial^2}{\partial z^2}\right)^{-1}\left(2 - L_1 + \frac{1}{\Delta s}\left(\frac{\partial^2}{\partial z^2}\right)^{-1}(1-L_1)\right) \tag{17}$$

$$L_3 = -\left(\frac{\partial^2}{\partial z^2}\right)^{-1}\left(1 + \frac{1}{\Delta s}\left(\frac{\partial^2}{\partial z^2}\right)^{-1}(1-L_1)\right) \tag{18}$$

Like the BDF2, the EDF2 requires a single-step scheme to initialize the algorithm.

B. Complementary Diffusion Equation

As mentioned in the Introduction, several authors such as Matsen[23], and Meng et al.[30] observed difficulties obtaining accurate values for the free energy, fields, and densities for grafted polymer brushes, which they attributed to the Dirac delta function in the initial condition for the complementary propagator. Below we present a smearing method that is used to resolve the initial condition for the complementary propagator for the one dimensional planar system. In this method, the grafting points are smeared over a finite-width function.

C. Smeared Distribution of Grafting Points

For the one dimensional case, setting $s = 0$ and substituting $q_{\mathbf{x}_\perp}(z, 0; [\mu_K]) = \delta(z - \epsilon)$ for $\epsilon \to 0+$ into Eqs. (7) and (8), the initial conditions for the complementary propagators take the following form

$$q_c(z, 0; [\mu_A]) = \frac{f\bar{L}_z}{\mathcal{Q}(\epsilon; [\mu_A])}\delta(z - \epsilon), \tag{19}$$

$$q_c(z, 0; [\mu_B]) = \frac{(1-f)\bar{L}_z}{\mathcal{Q}(\epsilon; [\mu_B])}\delta(z - \epsilon). \tag{20}$$

One can directly apply this initial conditions, which is associated with a source distribution, by approximating the Dirac delta function as a Kronecker delta function or by performing an approximate analytic propagation of the initial condition for one contour step[23,30]. We adopt the latter approach here in all results labeled "source" – namely, we apply the operator splitting formula (OSM) for a single contour step in tandem with the Green's function for the heat equation with either Dirichlet or Neumann boundary conditions to deduce the form of $q_c(z, \Delta s)$.

Since the main complication with the initial condition for the complementary propagator arises from an inability to numerically resolve the Dirac delta function, one way to avoid these complications would be to smooth out the function. A convenient choice is to approximate the Dirac delta function as a Gaussian centered around $z = \epsilon$ with a variance α:

$$q_{\mathbf{x}_\perp}(z, 0; [\mu_K]) \approx \frac{\exp[-(z-\epsilon)^2/(2\alpha)]}{\sqrt{\pi\alpha/2}}, \tag{21}$$

which is normalized such that:

$$\int_\epsilon^\infty dz \, \frac{\exp[-(z-\epsilon)^2/(2\alpha)]}{\sqrt{\pi\alpha/2}} = 1. \tag{22}$$

The Dirac delta function is then recovered in the limit of $\alpha \to 0$. This technique is similar to connecting the polymer chains to the surface using a stiff harmonic potential[21]. By using this approximation, the grafting points are no longer constrained to the surface at $z = \epsilon$, but are instead smeared over a half Gaussian.

Although the Gaussian satisfies the boundary condition at $z = 0$ (in the limit of $\epsilon \to 0$) it does not always satisfy the reflective boundary conditions at $z = \bar{L}_z$:

$$\frac{\partial}{\partial z}\left[\frac{\exp[-z^2/(2\alpha)]}{\sqrt{\pi\alpha/2}}\right]_{z=\bar{L}_z} = -\frac{\bar{L}_z \exp[-\bar{L}_z^2/(2\alpha)]}{\alpha\sqrt{\pi\alpha/2}}, \tag{23}$$

To rectify this, a small term can be added to the initial condition

$$q_{\mathbf{x}_\perp}(z, 0; [\mu_K]) = \frac{\exp[-z^2/(2\alpha)]}{\sqrt{\pi\alpha/2}} + \frac{z^2 \exp[-\bar{L}_z^2/(2\alpha)]}{2\alpha\sqrt{\pi\alpha/2}}, \tag{24}$$

which is exponentially small for large $\bar{L}_z$ or small α. Several different formulations of this term can be employed, but for moderately small values of α, such as $\alpha = 0.01$, it is essentially equal to zero, and in the limit of $\alpha \to 0$, the Dirac delta function is recovered.

Plugging this expression into Eq. (4), the partition function for the one component system takes the following form

$$Q[\mu_K] = \int_{\bar{L}_z} dz \left[\frac{\exp[-z^2/(2\alpha)]}{\sqrt{\pi\alpha/2}} + \frac{z^2 \exp[-\bar{L}_z^2/(2\alpha)]}{2\alpha\sqrt{\pi\alpha/2}} \right] q(z, 1; [\mu_K]). \tag{25}$$

Using this form of the partition function, along with the Gaussian approximation, the initial condition for the complementary propagator of the one component system becomes

$$q_c(z, 0; [\mu_K]) = \frac{f_K \bar{L}_z \exp[-z^2/(2\alpha)] + f_K \bar{L}_z z^2 \exp[-\bar{L}_z^2/(2\alpha)]/(2\alpha)}{\int_{\bar{L}_z} dz \left[\exp[-z^2/(2\alpha)] + z^2 \exp[-\bar{L}_z^2/(2\alpha)]/(2\alpha)\right] q(z, 1; [\mu_L])} \tag{26}$$

where the spatial integral can be calculated spectrally.

In situations where the masking method is used, rather than using a Gaussian it is more desirable to smear the grafting points over the width of the wall. Such a grafting distribution removes the additional variable α associated with the Gaussian method, thus simplifying the parameter space. A simple approach is to approximate the Dirac delta function as the square of the first derivative of the wall volume fraction located at the grafting surface, $\phi'_{w1}(z)$, where the prime denotes the first derivative in respect to z. This approximation assumes that the grafting points are distributed with a probability density proportional to $(\phi'_{w1}(z))^2$

$$q_{\mathbf{x}_\perp}(z, 0; [\mu_K]) = \frac{(\phi'_{w1}(z))^2}{\int_{\bar{L}_z} dz (\phi'_{w1}(z))^2}, \tag{27}$$

which is normalized to unit area. As in the case of the Gaussian approximation, this method modifies the form of the single chain partition function which is now given by

$$Q[\mu_K] = \frac{1}{\int_{\bar{L}_z} dz' (\phi'_{w1}(z'))^2} \int_{\bar{L}_z} dz (\phi'_{w1}(z))^2 q(z, 1; [\mu_K]). \tag{28}$$

This leads to the following form for the initial condition for the complementary propagator

$$q_c(z, 0; [\mu_K]) = \frac{f_K \bar{L}_z (\phi'_{w1}(z))^2}{\int_{\bar{L}_z} dz' (\phi'_{w1}(z'))^2 q(z', 1; [\mu_K])}. \tag{29}$$

This wall smearing could be conducted in a slightly different way. In the source distribution, we have assumed that each chain end is grafted at exactly the same plane ($z = \epsilon$). However, since the masking method allows us to model the surface as a diffuse substrate

with a certain transition width, we could also distribute the grafting ends throughout the wall transition. In this case, $q_{\mathbf{x}_\perp}(z,0;[\mu_K])$ and $Q_{\mathbf{x}_\perp}[\mu_K]$ for the chain grafted at $\mathbf{x}_\perp$ take the same form of those for a source distribution, but $q_c(z,0;[\mu_K])$ has an additional factor to account for the normalized grafted ends distribution function $g(z)$.

$$q_c(z,0;[\mu_K]) = \int_{\bar{A}} d\mathbf{x}_\perp \frac{f\bar{V}g(z)}{\bar{A}\mathcal{Q}(\mathbf{x}_\perp;[\mu_A])} q_{\mathbf{x}_\perp}(\mathbf{x},0;[\mu_A]). \tag{30}$$

We can choose the same distribution function as before $g(z) = \frac{(\phi'_{w1}(z))^2}{\int_{\bar{L}_z} dz(\phi'_{w1}(z))^2}$, which leads to

$$q_c(z,0;[\mu_K]) = \frac{f_K \bar{L}_z}{q(z,1;[\mu_K])} \frac{(\phi'_{w1}(z))^2}{\int_{\bar{L}_z} dz(\phi'_{w1}(z))^2}. \tag{31}$$

Although the resulting $q_c(z,0;[\mu_K])$ has a different normalizing denominator than Eq (29), we obtained very similar numerical results independent of which wall smearing method is used. As a consequence, for simplicity, we only have used the first smearing method in this paper.

D. Quadrature for Local Volume Fraction

To numerically calculate the local volume fraction for the A and B component defined in Eq. (9), a fourth-order accurate open extended formula[40,47] is used

$$\begin{aligned}\int_0^1 f(s)ds = \Delta s \Big[&\frac{55}{24}f(s_1) - \frac{1}{6}f(s_2) + \frac{11}{8}f(s_3) \\ &+ f(s_4) + f(s_5) + ... + f(s_{N_s-5}) + f(s_{N_s-4}) \\ &+ \frac{11}{8}f(s_{N_s-3}) - \frac{1}{6}f(s_{N_s-2}) + \frac{55}{24}f(s_{N_s-1})\Big] + \mathcal{O}(\Delta s^4).\end{aligned} \tag{32}$$

The open-quadrature excludes the end points, and consequently the (integrable) $\sim s^{-1/2}$ singularity at $s = 0$ which is observed for the source point distribution of grafting points. When the grafting points are adequately smeared the singularity at $s = 0$ is avoided, and closed-quadrature schemes can be used to accurately calculate the density.

E. Field Relaxation

To determine the field configurations $\mu_+^*(z)$ and $\mu_-^*(z)$ that correspond to the mean-field solution for this system, it is necessary to solve the saddle point equations given in Eqs. (10)

and (11). To solve these nonlinear equations, we employ the method of continuous steepest descent, where we introduce a fictitious time variable t, and relax in the direction of the field-gradient of the Hamiltonian. For this particular system the saddle point search is a *steepest ascent* in μ_+ and a *steepest descent* in μ_-. We use the following equations to obtain the saddle point configurations for μ_+^* and μ_-^*:

$$\frac{\partial}{\partial t}\mu_+(z,t) = \frac{\partial H[\mu_+,\mu_-]}{\partial \mu_+}, \tag{33}$$

$$\frac{\partial}{\partial t}\mu_-(z,t) = -\frac{\partial H[\mu_+,\mu_-]}{\partial \mu_-}. \tag{34}$$

To numerically implement these two equations, we can use the explicit forward Euler method which takes the following form:

$$\mu_+^{n+1}(z) = \mu_+^n(z) + \Delta t \frac{\partial H[\mu_+,\mu_-]}{\partial \mu_+}, \tag{35}$$

$$\mu_-^{n+1}(z) = \mu_-^n(z) - \Delta t \frac{\partial H[\mu_+,\mu_-]}{\partial \mu_-}, \tag{36}$$

both of which can be followed by a constant shift to center the fields around zero and improve stability. Here the superscript n denotes steps in the ficticious time variable t. Although this scheme is easily implemented, the algorithm's poor stability significantly restricted the size of the time step Δt that could be employed.

Ceniceros and Fredrickson proposed a more stable semi-implicit-Seidel (SIS) algorithm for a periodic system[3]. In this approach, the random phase approximation is used to expand the density operators (field gradients) to first order in $\mu_\pm$, then the linear terms are added and subtracted at the future and present time step, respectively, to produce the following algorithm:

$$\frac{\mu_+^{n+1} - \mu_+^n}{\Delta t} = -g * \mu_+^{n+1} + \frac{\partial H[\mu_+^n,\mu_-^n]}{\partial \mu_+^n} + g * \mu_+^n, \tag{37}$$

$$\frac{\mu_-^{n+1} - \mu_-^n}{\Delta t} = -(2/\chi N)\mu_-^{n+1} - \frac{\partial H[\mu_+^{n+1},\mu_-^n]}{\partial \mu_-^n} + (2/\chi N)\mu_-^n. \tag{38}$$

where the asterisk denotes a spatial convolution and g is the Debye scattering function. For the periodic system, the Debye function in Fourier-space is expressed as:

$$\hat{g}(k) = 2\bar{\phi}(e^{-k^2} + k^2 - 1)/k^4, \tag{39}$$

where k is the magnitude of the Fourier wavevector. Although this form of the Debye function is not appropriate for grafted chains, since it is obtained by performing the RPA on a non-tethered homopolymer in a periodic cell, it can still be used in the semi-implicit-Seidel update for the brush system. Using this approximate form of the Debye function in the saddle point update algorithm will not affect the final field configuration, but in some cases can increase the stability of the scheme.

As the simulation time (iteration number) increases, the fields configurations are updated based on Eqs. (33) and (34) until our convergence criterion is met, which is when the error is at machine precision. The error is defined as the l_1 norm of the sum of the saddle point equations, Eqs. (10) and (11), which gives

$$\begin{aligned} \text{error} = \frac{1}{N_z}\sum_{j=0}^{N_z-1} & |\phi_{\mathrm{A}}(z_j)+\phi_{\mathrm{B}}(z_j)-1| \\ & +|(2f-1)+2W(z_j)/\chi N-\phi_{\mathrm{A}}(z_j)+\phi_{\mathrm{B}}(z_j)|, \end{aligned} \tag{40}$$

and

$$\begin{aligned} &\text{error} = \\ &\frac{1}{N_z}\sum_{j=0}^{N_z-1}\left|\left(-\frac{2}{\chi N+2\zeta N}\mu_+(\mathbf{x})-\frac{2\zeta N}{\chi N+2\zeta N}\phi(\mathbf{x})\right)\right| \\ &+|(2f-1)+2W(z_j)/\chi N-\phi_{\mathrm{A}}(z_j)+\phi_{\mathrm{B}}(z_j)|, \end{aligned} \tag{41}$$

for the incompressible and compressible models, respectively. Self-consistency is achieved exactly when the error equals zero.

IV. RESULTS AND DISCUSSION

All of the methods above were implemented in FORTRAN 90 on a 2.00 GHz Intel Xeon CPU, where the discrete cosine (DCT-I) and sine (DST-I) transforms were performed using the FFTW package[10]. The initial field configurations were composed of random numbers uniformly distributed over [-0.5,0.5], unless otherwise noted, and the same initial field configuration was used for each individual study. In conducting field relaxations, the time step was selected to be as large as allowed by the stability of method.

For brevity, we introduce a shorthand notation to identify the various approaches, models, and boundary conditions. We have 8 different cases dependent on the compressibility,

boundary condition, and the distribution of grafting points. To identify these cases, a tag derived from a combination of three words is used, which indicate either an incompressible (incomp) or compressible (comp) model, whether Neumann (cosine) or Dirichlet (sine) boundary conditions are imposed, and if we are considering a source (source) or smeared (smear) distribution. For example, an incompressible symmetric binary melt brush where Neumann boundary conditions are considered in the z-direction with a source distribution of grafting points is labeled *incomp_cosine_source*. For situations where we consider both a source and smeared distribution, the last index is omitted, e.g. *incomp_cosine*.

A. Solving the Modified Diffusion Equation

In general, we find that the operator splitting method (OSM) is better suited to solve the modified diffusion equation for grafted systems than either the BDF or EDF algorithms due to the OSM's superior handling of large peaks in the fields μ_A and μ_B near the grafting surface at $z = 0$. When Neumann boundary conditions are considered, the large peaks have amplitude $\mathcal{O}(10)$. This is demonstrated for a one-component incompressible brush in Figure 1. The results are very similar for a two-component mixed brush system.

Although the field theory model is known to be invariant to a constant shift, μ_0, in the field, which allows a uniform shift to be subtracted at each field update to add stability, when this shift is employed with the BDF or EDF method there is an accumulation of numerical error which prevents driving the error to machine precision. The operator splitting method avoids this problem since the numerical algorithm involves only the exponential of the field such that a constant shift manifests in $\mathcal{Q}[\mu]$ as a multiplicative factor $\exp[-\mu_0 \Delta s]$. This factor cancels out exactly when calculating the density $-(1/\mathcal{Q}[\mu])\partial\mathcal{Q}[\mu]/\partial\mu$ using OSM, but when BDF or EDF are applied, the cancellation is not exact and numerical error accumulates at each field iteration. When the constant shifts are removed, the BDF and EDF methods are capable of producing converged solutions with an error of $\mathcal{O}(10^{-13})$, but the spatial average of the fields tends to drift away from the origin as shown in Figure 1. Although we have also observed drifts in the field in non-tethered systems, the magnitude of the drift is much larger in polymer brushes. This field drift can lead to very large or very small values of the single chain partition function and propagators depending on the direction of the drift towards either large positive or negative values. As a consequence, the BDF and EDF are

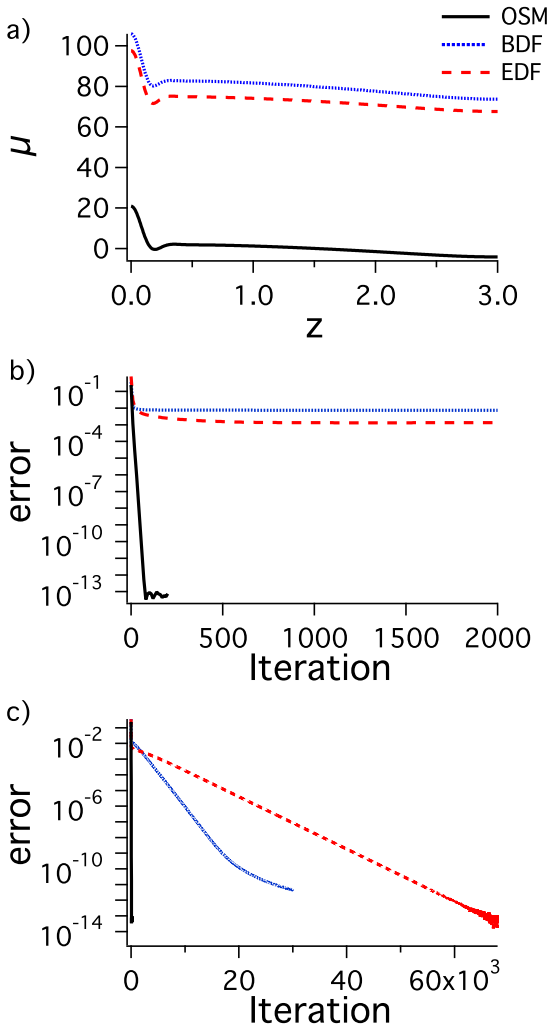

FIG. 1. (a) Comparison of the converged field μ for an incompressible one-component brush (reflective boundary conditions and source distribution) where the modified diffusion equation is solved using either the OSM, BDF, or EDF method, and the fields are not shifted. The error when the fields are (b) shifted or (c) not shifted. System parameters are $\bar{L}_z = 3$, $N_z = 512$, and $N_s = 256$.

problematic algorithms for conducting SCFT studies of polymer brushes.

B. Complementary Diffusion Equation and Grafting Point Smearing

As was described above, one approach to resolving the problematic initial condition for the complementary propagator is to replace the Dirac delta function by a half-Gaussian

distribution. Here we report results for such a smeared Gaussian distribution in the case of Neumann boundary conditions (cosine basis functions), and results obtained using a smearing distribution function constructed from the wall derivative for the case of Dirichlet boundary conditions (sine basis functions + masking method). Results from the source distribution will also be presented for comparison purposes.

In Figure 2, the converged fields and volume fractions, respectively, are shown for the incomp_cosine_source and comp_cosine_source cases. Unlike an untethered binary melt that exhibits macrophase separation, the grafted system can only microphase separate due the surface tethering of the polymers. The labels of A and B are arbitrary since the symmetry in chain length and composition produces a bi-stable system. In both compressible and incompressible systems, the configuration that the system adopts is due to an optimal balance between enthalpic repulsion of dissimilar segments and conformational entropy penalties associated with chain stretching. An optimal configuration of the fields μ_A and μ_B, minimizes the total mean-field free energy of the system. The rapidly varying features in μ_A and μ_B near $z = 0$ are a manifestation of the forces of constraint attempting to minimize density variations and overcrowding near the grafting surface. Since the magnitude of μ_A is greater than that of μ_B at the surface, the A polymers are repelled with a greater force at the wall and thus the A polymers are forced to stretch away from the grafting surface towards the grafting-free surface at $z = \bar{L}_z = 3$. Around $\bar{L}_z = 2$ the value of μ_B becomes greater than μ_A, which constrains the B polymers to the region near the grafting surface.

Although the density and field profiles for the incompressible and compressible cases exhibit similar behavior, slight differences are observed near the grafting surface. We observe that for the compressible model both A and B density profiles exhibit cusps near the grafting surface. The cusp in the density profiles is somewhat suppressed in the corresponding incompressible model since it produces a total density that exceeds one. In addition, the compressible model reduces the height of the first peak and damps a secondary u-shaped peak in the field profiles, both of which embody the repulsion of the polymers from the grafting wall.

When the grafting points are smeared over a Gaussian, the results from smeared simulations match those of the source approach when the variance, α, approaches 0, as seen in Figure 3 for the comp_cosine_smear case. As the value of the variance increases, which corresponds to the smearing of grafting points over a Gaussian of larger width, the rapidly

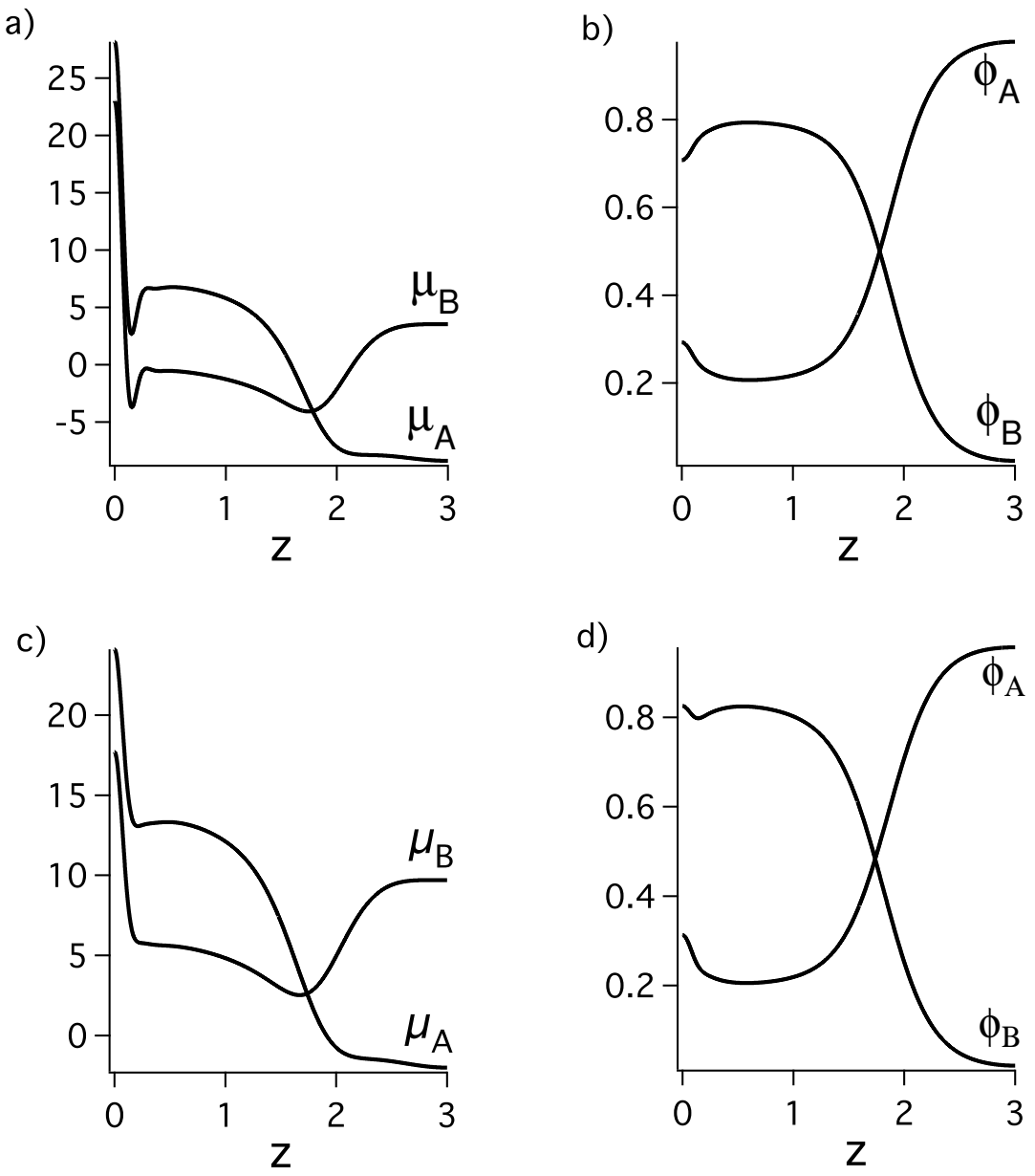

FIG. 2. Equilibrium configuration of $\mu_{A/B}$ (left) and $\phi_{A/B}$ (right) for (a,b) incomp_cosine_source and (c,d) comp_cosine_source cases. System parameters are $f = 0.5$, $\chi N = 12.5$, $\zeta N = 100$, $\bar{L}_z = 3$, $N_z = 4096$, and $N_s = 400$.

varying features in the fields μ_A and μ_B near $z = 0$ are suppressed, while the remainder of the field profiles are relatively unaffected. This field suppression manifests localized changes in the density profiles near the grafting substrate as seen in Figure 3, while the larger scale density features are seen to be relatively insensitive to changes in α.

When a confinement wall is modeled using the masking method with a sine basis and a

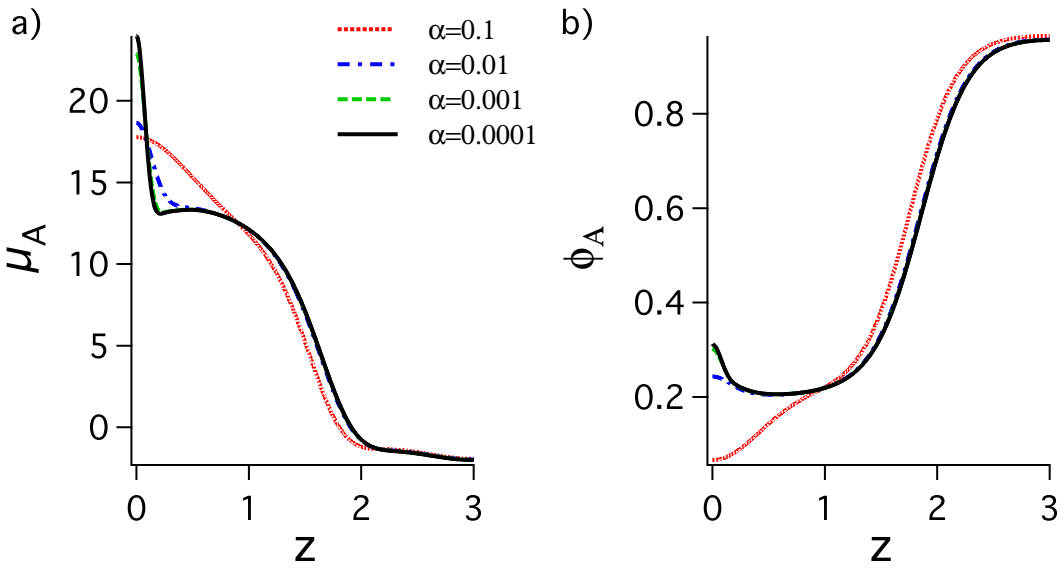

FIG. 3. Equilibrium configurations for μ_A and ϕ_A for the comp_cosine_smear case. System parameters are $f = 0.5$, $\chi N = 12.5$, $\zeta N = 100$, $\bar{L}_z = 3$, $N_z = 4096$, and $N_s = 400$.

source grafting distribution, we obtain similar trends for the fields and local volume fractions. This is shown in Figure 4 for the incomp_sine_source and comp_sine_source cases and a wall transition region of width $d = 0.01$. Due to the Dirichlet boundary conditions, the local volume fraction is forced to be zero at $z = 0$ and $z = \bar{L}_z$. Because of this and the incompressibility requirement, μ_A and μ_B assume large negative values near the boundaries, which attracts segments to satisfy the specified total density profile near the two boundaries. In the absence of the incompressibility constraint, we observe a depletion layer, where the total density $(\phi_A + \phi_B + \phi_{w1} + \phi_{w2})$ deviates from one near the boundaries (see Figure 4 d). In the limit of $\zeta \to \infty$ where the compressible model approaches the incompressible model, large negative field values with magnitude $\mathcal{O}(-10^2)$ are observed near the walls. These features are notably suppressed in the compressible model (e.g. for $\zeta N = 100$ field values are $\mathcal{O}(-10)$).

When walls of different widths are used to smear the grafting points, we do not expect to see convergence in d (as was observed upon reducing the Gaussian variance α in the Neumann case) since different wall profiles will produce different field and density profiles. Although the field values do not converge as d decreases, for small enough d the field profile does match that obtained using the source distribution as shown in Figure 5 for μ_A. The broader the

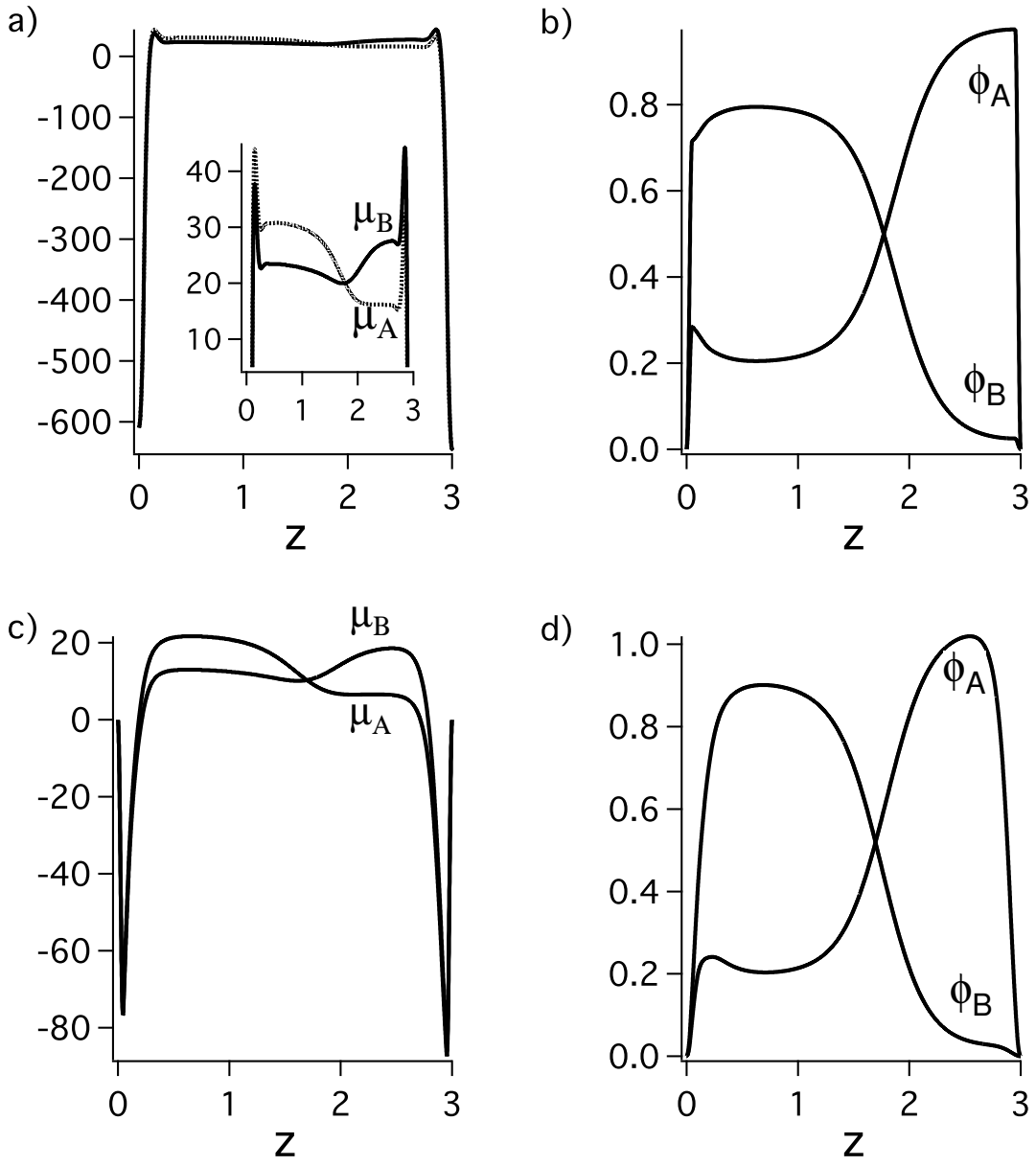

FIG. 4. Equilibrium configuration of $\mu_{A/B}$ (left) and $\phi_{A/B}$ (right) for (a,b) incomp_sine_source and (c,d) comp_sine_source cases. System parameters are $d = 0.05$, $f = 0.5$, $\chi_{w1}N = 0$, $\chi_{w2}N = 0$, $\zeta N = 100$, $\bar{L}_z = 3$, $N_z = 4096$, and $N_s = 400$.

wall profile becomes (increasing d), the further the grafting profile deviates from a source distribution, and larger discrepancies are observed between the two field profiles. In Figure 5, we observe substantial differences in μ_A between the source and smeared distributions for $d = 0.5$, while the source and smeared fields coincide at $d = 0.05$ for both the incompressible and compressible systems. Although the fields are sensitive to the value of d, the local

volume fractions outside the surface boundary layers are relatively insensitive to the width of the wall transition region.

C. Local Volume Fraction Quadrature

As mentioned in Section III D, the local volume fraction was calculated using an open composite quadrature formula, which omits the integrable $\sim s^{-1/2}$ singularity. Although this quadrature scheme is fourth-order accurate, the observed order is limited by the order of the operator-splitting method, which is second-order accurate. When the quadrature formula is used with a broad, smeared distribution of grafting points such as for $\alpha = 0.1$, and a prescribed (smooth) potential field, we observe an order of approximately 2, as shown in Figure 6. This order is calculated using the error defined as $max_i|\phi(x_i, N_s; [\mu]) - \phi(x_i, N_s = 10000; [\mu])|$. As the value of α is decreased to approach a source distribution, the observed order drops significantly to ≈ 1. This reflects a slow convergence of the fields, and consequently the density, with the chain contour resolution N_s. As the grafting points are adequately smeared, faster convergence with N_s is observed. This behavior is also observed for the incomp_sine_smear and comp_sine_smear cases when the width of the wall transition region approaches zero, $d \to 0$. The convergence of the field with N_s is further discussed in the following section.

D. Spatial and Contour Resolution Dependence of the Free Energy

In the case of a source distribution of grafting points, we have seen that a cusp is produced in the self-consistent fields near the grafting surface that contributes to a host of numerical problems including slow convergence with respect to field updates and subsequently the free energy. Matsen and Griffiths[27] observed similar behavior with the fully spectral method and Neumann boundary conditions, where they showed that the free energy converged slowly with the number of basis functions. Although this problem is manifest when absolute free energies are desired, these authors observed that relative free energies between two phases can be accurately calculated since numerical errors affect each phase in a similar manner when compared using the same number of basis functions.

In Figure 7, we observe relatively rapid convergence of the absolute free energy with

increased spatial resolution N_z when smeared distributions are employed. Special care should be taken to ensure that N_z is sufficient to adequately capture the sharp peaks in the field profiles, although we have observed that the local volume fraction and field configuration are relatively insensitive to N_z provided this condition is met. The insensitivity of volume fraction profiles to N_z was also noted by Matsen and Griffiths [27]. Figure 7 shows the magnitude of the free energy plotted against N_z, where the free energy was shifted for visual comparison so that its value calculated at the lowest spatial resolution is zero. As seen in Figure 7, faster convergence is observed for compressible and incompressible models and both types of boundary conditions when the grafting points are smeared. This is again due to the smoother field profiles produced by the smeared models.

We have observed a particularly slow convergence of both fields and free energy with the contour resolution, N_s when a source distribution is employed. This is observed in Figure 8, which shows the field profiles for the incomp_cosine and comp_cosine cases. The volume fraction profiles are omitted since they are similar, although they exhibit a weaker dependence on N_s. For both the incompressible and compressible models, the peak near the grafting source increases as the contour resolution increases with no signs of convergence when the grafting is modeled as a source distribution (Figures 8 a and c). When the grafting points are smeared over a Gaussian this dependence on the contour resolution is suppressed, and we observe markedly faster convergence in the field profile near the grafting surface as shown in Figure 8 b and d for a variance of $\alpha = 0.01$.

A more problematic sensitivity to N_s arises when Dirichlet boundary conditions are applied in tandem with wall masking. For the incompressible model, the peak in the field profile near the grafting source appears to increase with the contour resolution in a similar manner as we observed with incomp_cosine_source. By using a smeared distribution, we begin to observe convergence with N_s, but at a much slower rate than for incomp_cosine_smear (Figure 8 b and 9 b). This is due to the confinement wall, which also produces slow convergence with N_s in the case of confined *non-grafted* polymer melts such as those studied in Ref[14]. However, when the compressible model is applied to a non-grafted confined melt using the masking method, the fields quickly converge with N_s suggesting an incompatibility of the incompressibility constraint with the masking method. In Figure 9, we show configurations of μ_A in the wall region for the incomp_sine and comp_sine cases of a grafted binary brush, where the full field profile exhibits the same features as in Figure 4. Convergence is evidently

improved both by adopting a compressible model as well as by smearing the grafting points. Both steps tend to smooth the potential fields and damp the anomalous wall features.

Since the free energy (mean-field Hamiltonian) is dependent on the field configuration as seen in Equation 3, it also exhibits a dependence on the contour resolution. This is shown in Figure 10, where the magnitude of the free energy is plotted as a function of N_s and the same shift is performed as in Figure 7. For a source distribution of grafting points, the convergence is much slower than in the equivalent smeared case, and the rate of convergence increases with the width of the smearing. Between our four models (incomp_cosine, incomp_sine, comp_cosine, and comp_sine), the incomp_sine_source model exhibits the poorest behavior with no sign of convergence of the free energy up to $N_s = 800$. This poor behavior of the incomp_sine_source model is again due to the incompatibility of the confinement wall with the incompressibility constraint; switching to a compressible model speeds up convergence significantly.

Even though convergence of the absolute free energy requires large values for N_s, when comparing the stability of two phases only the difference in free energy, i.e. the "relative" free energy, is important. At fixed spatial resolution, we have observed that numerical errors associated with chain contour discretization tend to cancel in the relative free energy. Shown in Figure 11 are the free energies of mixed brushes at $\chi N = 12.5$ and $\chi N = 2.0$, and the relative free energy between the two states, plotted versus N_s for the incomp_sine_source and comp_sine_source cases. Although the absolute free energies converge very slowly with N_s, the relative free energy converges extremely rapidly with N_s for both compressible and incompressible models. This also proves true for a broader set of models with smeared distributions of grafting points and Neumann boundary conditions. We conclude that boundaries between phases that have been simulated at the same spatial resolution N_z can be accurately located by means of simulations with surprisingly small contour resolution N_s.

E. Field Relaxation

Our results up to this point suggest that both compressible and incompressible models, with either source or smeared grafting distributions, can be applied to mixed brush SCFT simulations if densities and relative free energies are the objects of primary interest. Nonetheless, one area where we observe significant differences between the models relates to

the difficulty of field relaxation. As should be expected, we observe significantly faster field convergence for the compressible system (vs. incompressible) when the sine basis and masking method are used to mimic a confining surface, and more rapid convergence of smeared models in comparison with source grafting models.

As discussed in Section III E, the potential fields can be updated by a continuous steepest descent using methods such as explicit forward Euler (FEU) and the semi-implicit-Seidel (SIS) method[3]. Although the SIS method is approximately twice as expensive as the FEU scheme for this binary brush system, the added stability of the method for some models can permit a larger update time step and thus faster convergence.

For the incomp_cosine and comp_cosine models, the SIS method allows the fields to relax significantly faster than the FEU method. In Figure 12, the FEU and SIS performance is compared for incomp_cosine_source, where similar convergence benefits were observed for a smeared distribution and for our comp_cosine systems. A maximum time step of $\Delta t = 6.4$ can be used with the explicit forward Euler method, where the error is reduced to 10^{-12} in 1250 iterations (cpu time = 1009.77 sec). With the more stable semi-implicit-Seidel scheme, the added stability allows the time step to be increased to $\Delta t = 140$, where an error of 10^{-12} can be obtained in 132 iterations (cpu time = 216.79 sec). In this case the SIS method effectively damps high frequency modes of the fields, improving stability and allowing for a larger time step. The high frequency mode damping also confers improved stability at the early stages of simulations that are initiated from (rough) random fields. It is notable that in the present implementation of SIS we do not use the exact kernel of the linearized force, but instead use an approximate (and cheaper to compute) form derived for a non-tethered binary blend. Nonetheless, the implemented SIS considerably outperforms the FEU method, which utilizes no information about the linear forces in the model.

While SIS outperforms FEU for Neumann boundary conditions, unfortunately when Dirichlet boundary conditions are imposed in tandem with a wall mask, the SIS scheme does not outperform the FEU, regardless of how the grafting points are distributed or whether an incompressible or compressible model is employed. This is not surprising since the boundary condition and the wall mask both affect the high frequency modes, such that the Debye function is no longer an accurate representation. In addition, the wall pressure anomaly is more severe (c.f. Figure 4) for the Dirichlet plus masking models relative to the Neumann models. We note that Hur et. al[14] was able to use the SIS method with a larger time step

than FEU for a similarly confined incompressible diblock copolymer melt utilizing Dirichlet plus masking, although the wall function was of a different shape than that employed here.

The FEU scheme for the Dirichlet case demonstrates significantly better convergence properties by using a compressible model vs. the incompressible model. For a system system with $\bar{L}_z = 3$, $f = 0.5$, $\chi N = 12.5$, $N_z = 4096$, $N_s = 400$, and $\zeta N = 100$, and with a source grafting distribution, we were able to decrease the error to machine precision in 81,000 and 480 iterations for the incompressible and compressible models, respectively, where we used a time step of 5.0 for the pressure and 1.0 for the exchange/composition fields. As steps 2-5 in Section III are iterated, the peak in the pressure field near the walls continuously increases in order to suppress the polymer segment density. This feature is relaxed by going to a compressible model and the smoother equilibrium pressure field is more rapidly attained.

Lastly, it has been previously observed that is very difficult to relax the fields for highly stretched brushes[23]. To produce a thicker brush requires that the grafting density also increase, which sharpens the impact of a source grafting distribution on the pressure anomaly. By smearing the grafting points, we are able to compensate this effect and thereby simulate thicker brushes. For a pure source distribution, brush thicknesses beyond $\approx 3R_{g0}$ become problematic, but even with moderate smearing ($\alpha = 0.5$), we have found it straightforward to converge SCFT simulations for brushes approximately $5R_{g0}$ in thickness. Although thicker brushes could in principle be simulated by employing broader smearing profiles, such systems are of limited experimental relevance.

V. CONCLUSIONS AND OUTLOOK

We have investigated a variety of numerical issues associated with the simulation of grafted AB binary brushes in the pseudo-spectral approach to SCFT. The grafting and free surfaces were modeled by using either Neumann boundary conditions, or Dirichlet boundary conditions coupled with a mask to specify diffuse boundaries for the polymer film. For both types of boundary conditions, our study was restricted to neutral surfaces for the A and B species, but the Dirichlet plus masking approach is more flexible in allowing for arbitrary surface affinities to be imposed. Several numerical problems were seen to arise from the Dirac delta function initial condition for the complementary chain propagator that relates

to the chain ends tethered at grafting surface. In particular, the need to accurately resolve and propagate this singular function leads to slow convergence in the fields, poor convergence of quadrature formulas to obtain the density operators, and a sensitivity of the potential fields and free energy to the chain contour resolution, N_s.

To address these numerical problems, we have considered grafted brush models that replace the Dirac delta function with a smeared distribution of grafting points normal to the grafting surface. This smearing can achieved, e.g., by approximating the Dirac delta function as a Gaussian with variance α centered at the grafting point. When the Dirichlet plus masking model is used, the grafting points can be conveniently smeared over the wall profile (of width d), so no additional smearing width parameters need be introduced. By smearing the grafting points, not only did we observe faster convergence in the free energy and field profiles, but we were also able to achieve approximately second-order accuracy in contour resolution for the density operators.

When the sine basis (Dirichlet conditions) is used in tandem with masking for an incompressible brush model, a singular feature is generated in the pressure field that slows convergence, particularly with respect to chain contour refinement. This behavior is not limited to brushes, but is also observed for non-tethered systems such as polymer melts. The problem can be resolved by employing a *compressible* melt model, which allows the density to adapt to tethering and constraint forces near a surface. For the mixed brush system, we have found that the pressure anomaly is greatly reduced by application of a compressible model and this has a dramatic effect on accelerating convergence, with respect to the number of field iterations as well as to space and contour resolution.

The numerical work reported here was restricted to one spatial dimension, although most applications of polymer brushes demand fully three-dimensional solutions and a flexible modeling platform that can accommodate a wide variety of wetting conditions at both grafting and free surfaces. All factors considered, the most robust and computationally efficient model for large-scale, three-dimensional SCFT simulations of mixed polymer brushes is the compressible model utilizing Dirichlet conditions plus masking and a smeared distribution of grafting points.

ACKNOWLEDGMENTS

This work was supported by NSF Grant No. DMR09-04499 and made use of MRL Central Facilities supported by the MRSEC Program of the NSF under Grant No. DMR05-20415. HDC was partially supported by NSF grant No. DMS10-16310.

REFERENCES

[1]U.M. Ascher, S.J. Ruuth, and R.J. Spiteri. Implicit-explicit runge-kutta methods for time-dependent partial differential equations. *Appl. Numer. Math.*, 25:151–167, 1997.

[2]A.W. Bosse, C.J. García-Cervera, and G.H. Fredrickson. Microdomain ordering in laterally confined block copolymer thin films. *Macromolecules*, 40(26):9570–9581, 2007.

[3]H.D. Ceniceros and G.H. Fredrickson. Numerical solution of polymer self-consistent field theory. *Multiscale Model. Simul.*, (3):452–474, 2004.

[4]S. Chandralekha, G.T. Pickett, and A.C. Balazs. Interactions between polymer-coated surfaces in poor solvents. 1. surfaces grafted with a and b homopolymers. *Macromolecules*, 29:7559–7570, 1996.

[5]S.M. Cox and P.C. Matthews. Exponential time differencing for stiff systems. *J. Comput. Phys.*, 176(2):430–455, 2002.

[6]P.G. de Gennes. Conformations of polymers attached to an interface. *Macromolecules*, 13(5):1069–1075, 1980.

[7]E.H. Feng, W.B. Lee, and G.H. Fredrickson. Supramoleciular diblock copolymers: A field-theoretic model and mean-field solution. *Macromolecules*, 40(3):693–702, 2007.

[8]G.H. Fredrickson, V.Ganesan, and F.Drolet. Field-theoretic computer simulation methods for polymer and complex fluids. *Macromolecules*, 35:16–39, 2002.

[9]G.H. Fredrickson. *The equilibrium theory of inhomogenous polymers.* Clarendon Press, Oxford, 2006.

[10]M.Frigo and S.G. Johnson. The design and implementation of FFTW3. *Proceedings of the IEEE*, 93(2):216–231, 2005.

[11]P.G. de Gennes. Scaling theory of polymer adsorption. *J. Phys.*, pages 1445–1452, 1977.

[12]D. Gottlieb and S.A. Orszag. *Numerical analysis of spectral methods: theory and applications.* Society for Industrial and Applied Mathematics (SIAM), Philadelphia, 1977.

[13]A. Halperin, M. Tirrell, and T.P. Lodge. Tethered chains in polymer microstructures. *Adv. Polym. Sci.*, 100:31–71, 1992.

[14]S.M. Hur, C.J. Garcia-Cervera, E.J. Kramer, and G.H. Fredrickson. Scft simulations of thin film blends of block copolymer and homopolymer laterally confined in a square well. *Macromolecules*, 42:5861–5872, 2009.

[15]W.K. Idol and J.L. Anderson. Effects of adsorbed polyelectrolytes on convective flow and diffusion in porous membranes. *J. Membr. Sci.*, 28(3):269–286, 1986.

[16]A.K. Kassam and L.N. Trefethen. Fourth-order time-stepping for stiff pdes. *SIAM J. Sci. Comput.*, 26(4):1214–1233, 2002.

[17]J.U. Kim and M.W. Matsen. Finite-stretching corrections to the milner-witten-cates theory for polymer brushes. *Eur. Phys. J. E*, 23:135–144, 2007.

[18]A.E. Likhtman and A.N. Semenov. An advance in the theory of strongly segregated polymers. *Europhys. Lett.*, 51(3):307–313, 2000.

[19]J.F. Marko and T.A. Witten. Phase-Separation in a Grafted Polymer Layer. *Phys. Rev. Lett.*, 66(11):1541–1544, 1991.

[20]M.W. Matsen. Thin films of block copolymer. *J. Chem. Phys.*, 106(18):7781–7791, 1997.

[21]M.W. Matsen. Corrections to the strong-stretching theory of polymer brushes due to the entropy of the free ends. *J. Chem. Phys.*, 117(5):2351–2358, 2002.

[22]M.W. Matsen. The standard gaussian model for block copolymer melts. *J. Phys.:Condens. Matter*, 14(2):R21–R47, 2002.

[23]M.W. Matsen. Investigating the dominant corrections to the strong-segregation theory for dry polymeric brushes. *J. Chem. Phys.*, 121(4):1938–1948, 2004.

[24]M.W. Matsen and F.S. Bates. Unifying weak- and strong-segregation block copolymer theories. *Macromolecules*, 29(4):1091–1098, 1996.

[25]M.W. Matsen and J.M. Gardiner. Autophobic dewetting of homopolymer on a brush and entropic attraction between opposing brushes in a homopolymer matrix. *J. Chem. Phys.*, 115(6):2794–2804, 2001.

[26]M.W. Matsen and J.M. Gardiner. Corrections to the strong-stretching theory of polymer brushes due to the proximal layer. *J. Chem. Phys.*, 118(8):3775–3781, 2003.

[27]M.W. Matsen and G.H. Griffiths. Melt brushes of diblock copolymer. *Eur. Phys. J. E*, 29(2):219–227, 2009.

[28]M.W. Matsen and M. Schick. Stable and unstable phases of a diblock copolymer melt.

Phys. Rev. Lett., 72(16):2660–2663, 1994.

[29]M.W. Matsen and M. Schick. Self-assembly of block copolymers. *Curr. Opin. Colloid Interface Sci.*, 1(3):329–336, 1996.

[30]D. Meng and Q. Wang. Solvent response of diblock copolymer brushes. *J. Chem. Phys.*, 130(13):134904–134904–9, 2009.

[31]S.T. Milner. Polymer brushes. *Science*, 251(4996):905–914, 1991.

[32]S.T. Milner, T.A. Witten, and M.E. Cates. Theory of the grafted polymer brush. *Macromolecules*, 21(8):2610–2619, 1988.

[33]S.T. Milner, T.A. Witten, and M.E. Cates. Effects of polydispersity in the end-grafted polymer brush. *Macromolecules*, 22(2):853–861, 1989.

[34]S.T. Milner, T.A. Witten, and Cates M.E. A parabolic density profile for grafted polymers. *Europhys. Lett.*, 5(5):413–418, 1988.

[35]M. Müller. Phase diagram of a mixed polymer brush. *Phys. Rev. E*, 65:030802–030802–4, 2002.

[36]J-R. Roan Attraction between nanoparticles induced by end-grafted homopolymers in good solvent. *Phys. Rev. Lett.*, 86:1027–1030, 2001.

[37]J-R. Roan Erratum: Attraction between nanoparticles induced by end-grafted homopolymers in good solvent. *Phys. Rev. Lett.*, 87:059902(E), 2001.

[38]C.B. Muratov, M. Novaga, G. Orlandi, and C.J. García-Cervera. *Geometric strong segregation theory for compositionally asymmetric diblock copolymer melts*, volume 9 of *CRM Series: Singularities in nonlinear evolution phenomena and applications*. Birkhauser, 2009.

[39]R.R. Netz and M. Schick. Polymer brushes: From self-consistent field theory to classical theory. *Macromolecules*, 31:5105–5122, 1998.

[40]W.H. Press, S.A. Teukolsky, W.T. Vetterling, and B.P. Flannery. *Numerical recipes in fortran 77: second edition*. Cambridge University Press, New York, NY, 1992.

[41]K.O. Rasmussen and G. Kalosakas. Improved numerical algorithm for exploring block copolymer mesophases. *J. Polym. Sci., Part B: Poly. Phys.*, 40:1777–1783, 2002.

[42]U.M. Ascher, S.J. Ruuth and B.T.R. Wetton. Implicit-explicit methods for time-dependent partial differential equations. *SIAM J. Numer. Anal.*, 32(3):797–823, 1995.

[43]J.J. Sakurai. *Modern quantum mechanics, revised edition*. Addison Wesley, Reading, MA, 1994.

[44]J.M.H.M. Scheutjens and G.J. Fleer. Statistical theory of the adsorption of interact-

ing chain molecules. 1. partition function, segment density distribution, and adsorption isotherms. *J. Phys. Chem.*, 83(12), 1619-1635 1979.

[45]A.N. Semenov. Contribution to the theory of microphase layering in block-copolymer melts. *Soviet Physics JETP*, 61:733–742, 1985.

[46]A. Sidorenko, S. Minko, K. Schenk-Meuser, H. Duschner, and M. Stamm. Switching of polymer brushes. *Langmuir*, 15:8349–8355, 1999.

[47]J. Stoer and R. Bulirsch. *Introduction to numerical analysis*. Springer-Verlag, New York, 1980.

[48]G. Strang. On the construction and comparision of difference schemes. *SIAM J. Numer. Anal.*, 5(3):506–517, 1968.

[49]G. Tzeremes, K.O. Rasmussen, T. Lookman, and A. Saxena. Efficient computation of the structural phase behavior of block copolymers. *Phys. Rev. E*, 65(4, Part 1):041806–041806–5, 2002.

[50]C.M. Wijmans and J.M.H.M Scheutjens. Self-consistent field theories for polymer brushes. lattice calculations and an asymptotic analytical description. *Macromolecules*, 25:2657–2665, 1992.

[51]T.A. Witten and P.A. Pincus. colloidal stabilization by long grafted polymers. *Macromolecules*, 19(10):2509–2513, 1986.

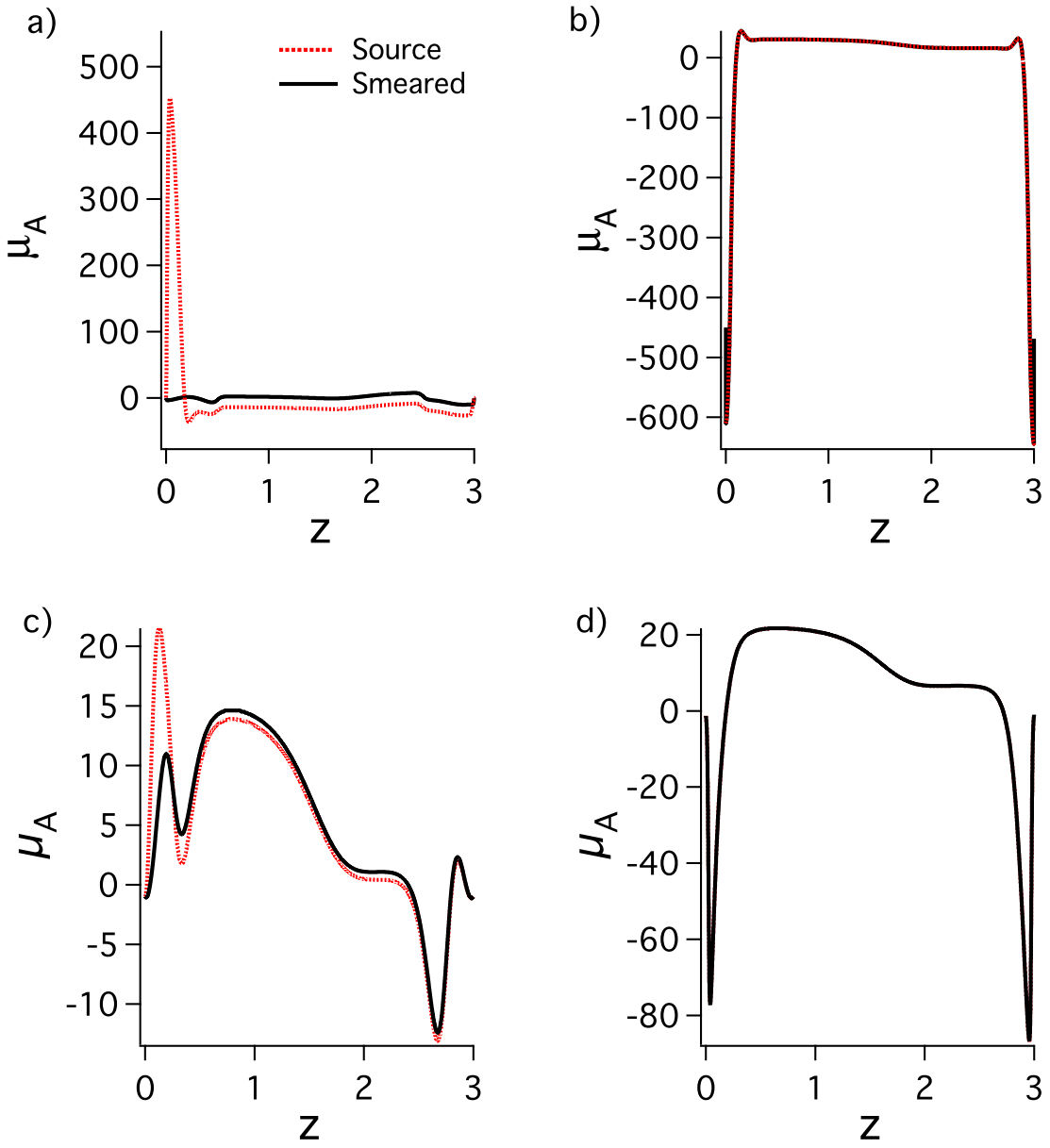

FIG. 5. Equilibrium configurations for μ_A, where the grafting points are smeared over a wall width of (a,c) $d = 0.5$ or (b,d) $d = 0.05$ for cases of (a,b) incomp_sine_smear and (c,d) comp_sine_smear. The profiles obtained using the source and smeared distribution are shown in red and black, respectively. System parameters are $f = 0.5$, $\chi N = 12.5$, $\chi_{w1}N = 0$, $\chi_{w2}N = 0$, $\zeta N = 100$, $\bar{L}_z = 3$, $N_z = 4096$, and $N_s = 400$.

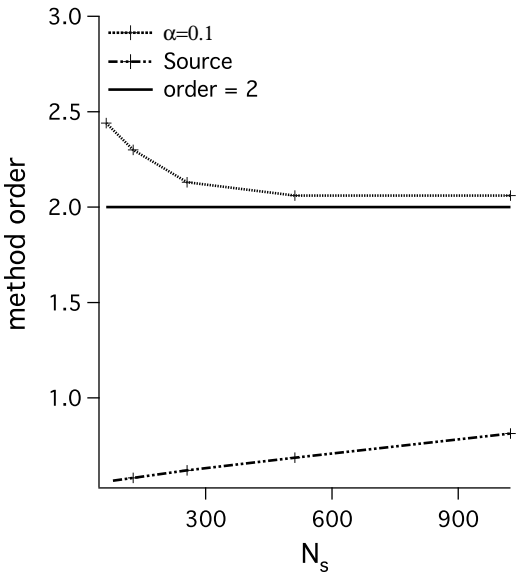

FIG. 6. Order observed in $\Delta s \sim 1/N_s$ for the third-order open ended formula for incomp_cosine. Both propagators were calculated using a specified smooth (cosine) potential field. The "exact" solution is obtained from a simulation with $N_s = 10000$. Parameters held constant in this study are $\bar{L}_z = 3$ and $N_z = 4096$.

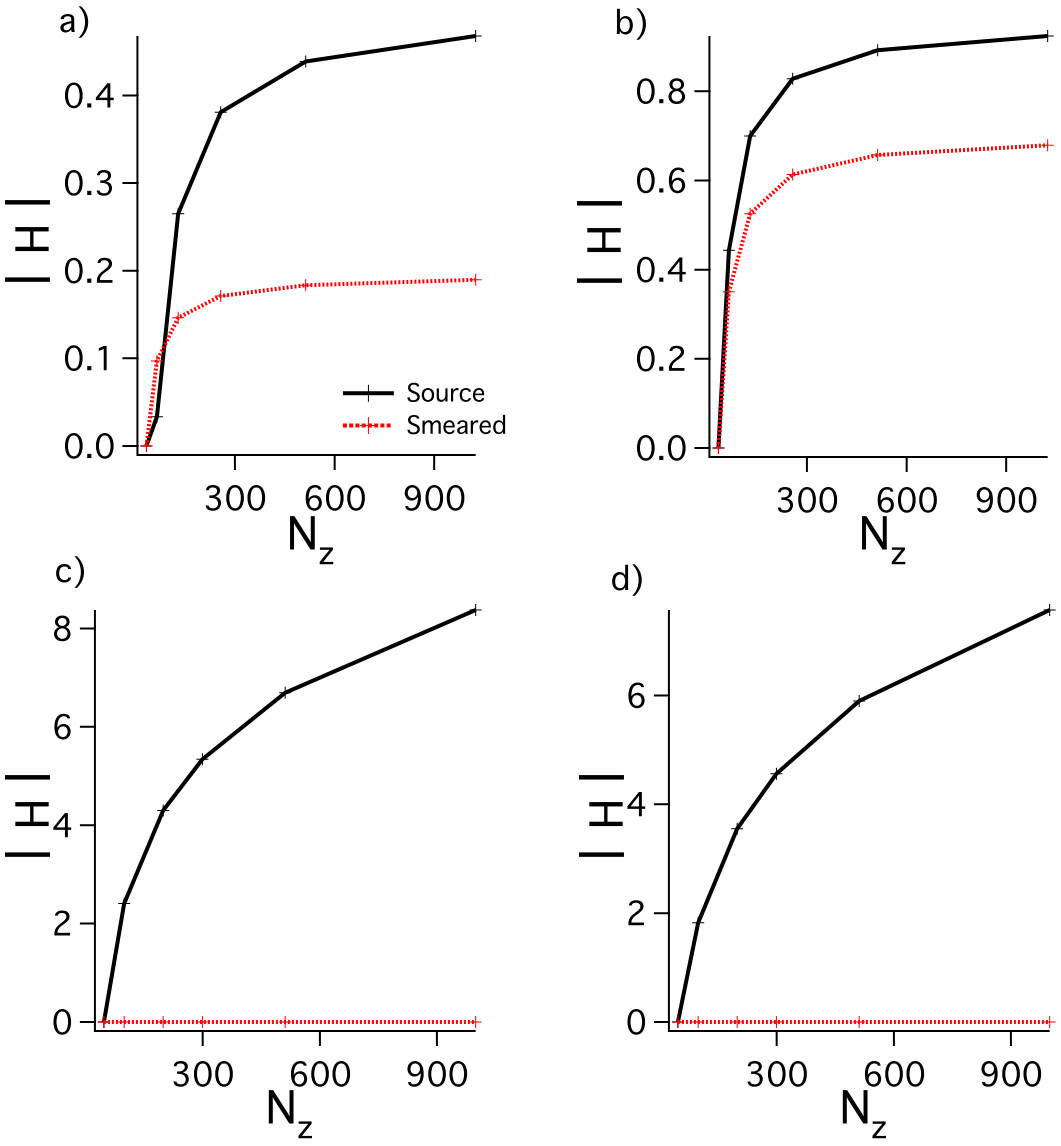

FIG. 7. The magnitude of the (shifted) free energy at $\chi N = 12.5$ vs N_z for the (a) incomp_cosine, (b) comp_cosine, (c) incomp_sine and (d) comp_sine cases. System parameters are $f = 0.5$, $\chi N = 12.5$, $\chi_{w1} N = 0$, $\chi_{w2} N = 0$, $\zeta N = 100$, $\alpha = 0.01$, $d = 0.5$, $\bar{L}_z = 3$, and $N_s = 400$.

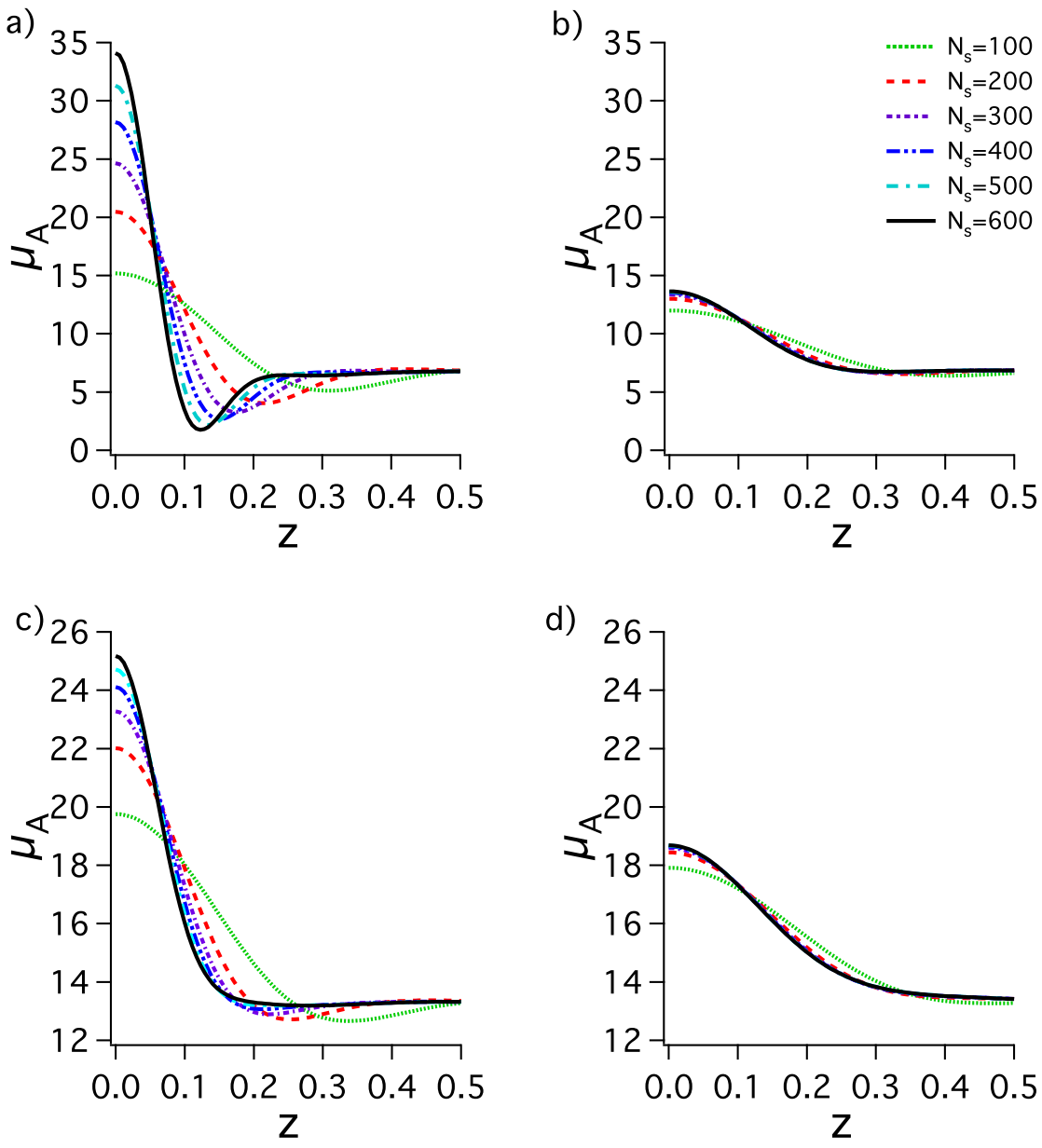

FIG. 8. Equilibrium configurations (zoomed in) for μ_A for different contour resolutions, N_s for (a) incomp_cosine_source (b) incomp_cosine_smear ($\alpha = 0.01$), (c) comp_cosine_source, and (d) comp_cosine_smear ($\alpha = 0.01$) cases. System parameters are $f = 0.5$, $\chi N = 12.5$, $\zeta N = 100$, $\bar{L}_z = 3$, and $N_z = 513$.

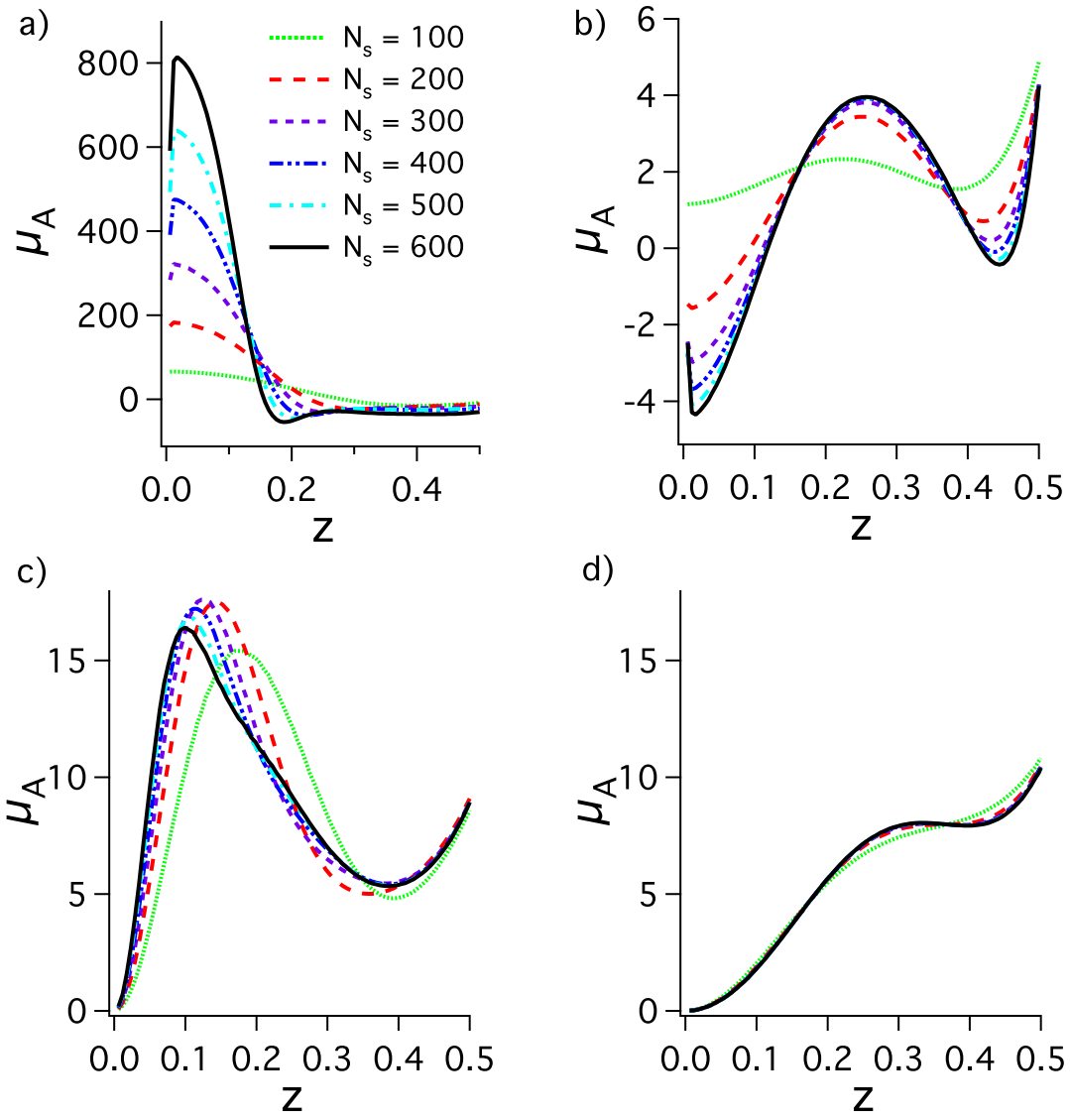

FIG. 9. Equilibrium configurations (zoomed in) of μ_A for varying contour resolution, N_s, for (a) incomp_sine_source, (b) incomp_sine_smear ($d = 0.5$), (c) comp_sine_source, and (d) comp_sine_smear ($d = 0.5$) cases. System parameters are $f = 0.5$, $\chi N = 12.5$, $\chi_{w1} N = 0$, $\chi_{w2} N = 0$, $\zeta N = 100$, $\bar{L}_z = 3$, and $N_z = 511$.

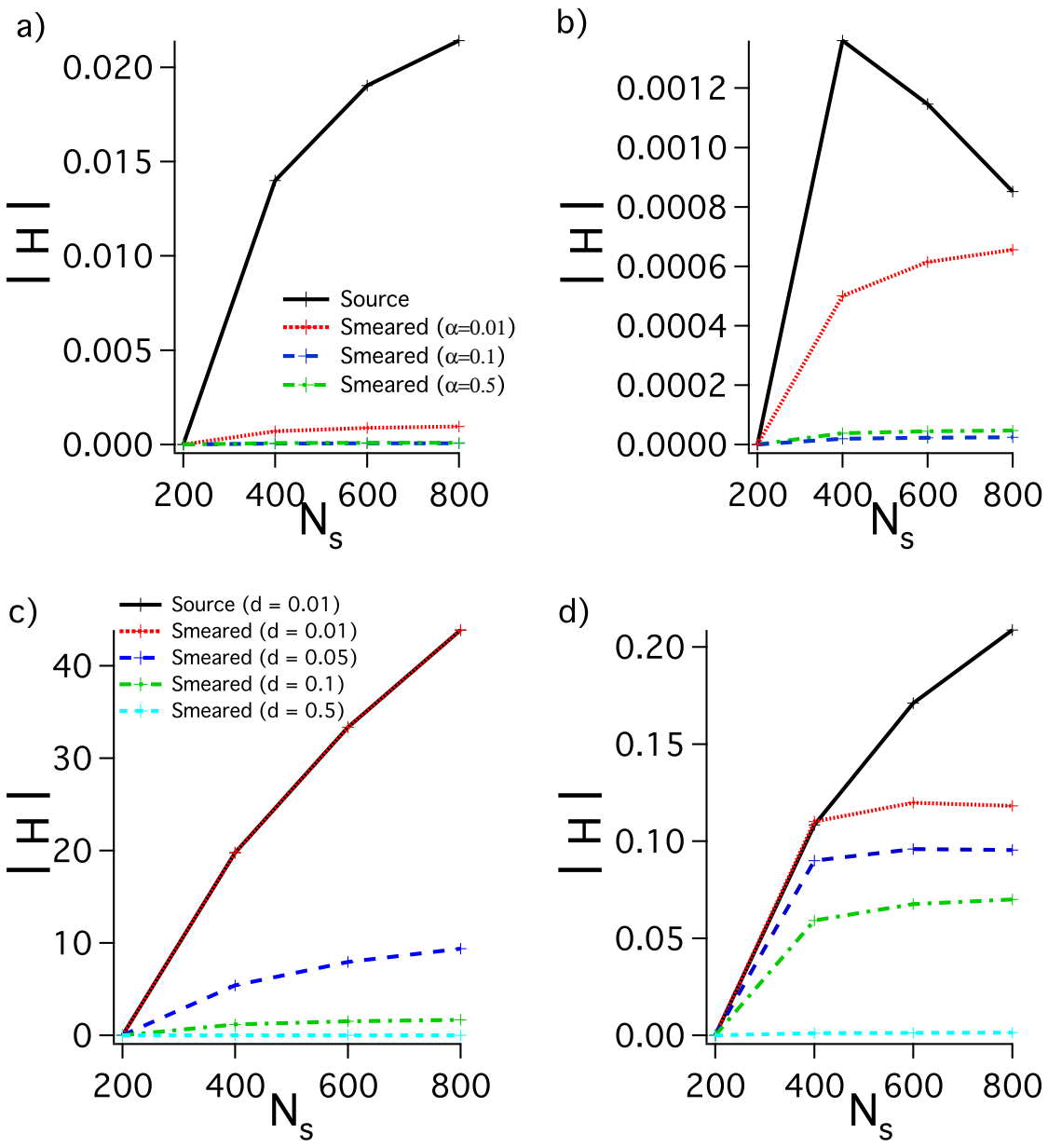

FIG. 10. Magnitude of the relative free energy vs. N_s for (a) incomp_cosine, (b) comp_cosine, (c) incomp_sine, and (d) comp_sine. System parameters are $f = 0.5$, $\chi N = 12.5$, $\bar{L}_z = 3$, $\chi_{w1}N = 0$, $\chi_{w2}N = 0$, $\zeta N = 100$, $\bar{L}_z = 3$, and $N_z = 4096$.

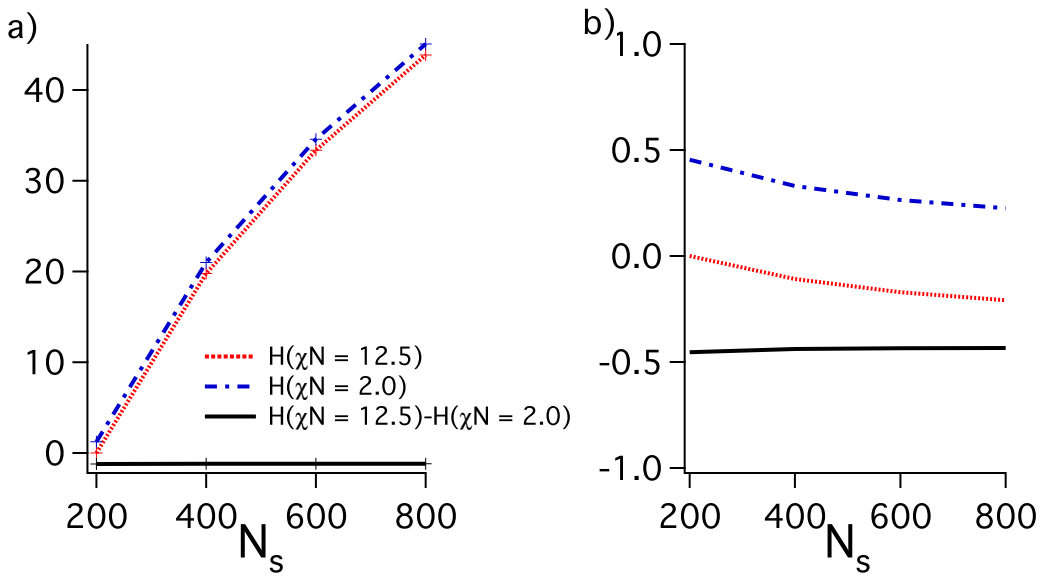

FIG. 11. Free energy at $\chi N = 12.5$ and $\chi N = 2.0$, and the relative free energy vs. N_s for (a) incomp_sine_source and (b) comp_sine_source cases. System parameters are $f = 0.5$, $\chi_{w1}N = 0$, $\chi_{w2}N = 0$, $\zeta N = 100$, $\bar{L}_z = 3$, and $N_z = 4096$.

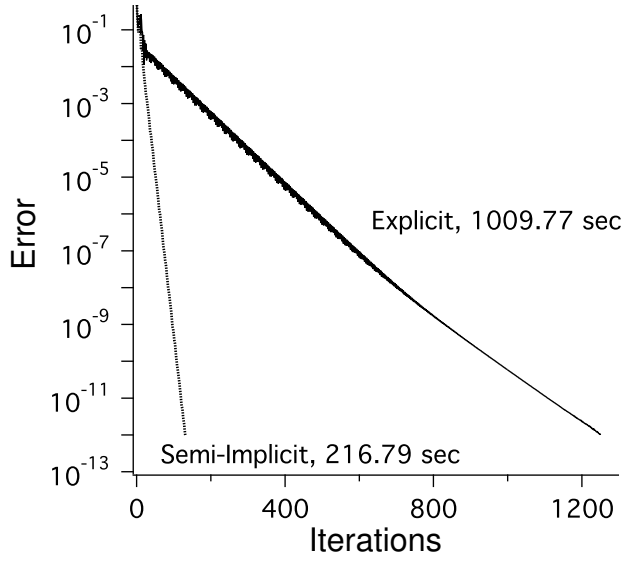

FIG. 12. Error vs. the number of iterations for a incompressible binary melt brush with a source distribution, Neumann boundary conditions and for two different update schemes: the forward Euler method and the semi-implicit-Seidel. System parameters are $f = 0.5$, $\bar{L}_z = 3$, $N_s = 400$, and $N_z = 4096$.